



저작자표시-비영리-변경금지 2.0 대한민국

이용자는 아래의 조건을 따르는 경우에 한하여 자유롭게

- 이 저작물을 복제, 배포, 전송, 전시, 공연 및 방송할 수 있습니다.

다음과 같은 조건을 따라야 합니다:



저작자표시. 귀하는 원저작자를 표시하여야 합니다.



비영리. 귀하는 이 저작물을 영리 목적으로 이용할 수 없습니다.



변경금지. 귀하는 이 저작물을 개작, 변형 또는 가공할 수 없습니다.

- 귀하는, 이 저작물의 재이용이나 배포의 경우, 이 저작물에 적용된 이용허락조건을 명확하게 나타내어야 합니다.
- 저작권자로부터 별도의 허가를 받으면 이러한 조건들은 적용되지 않습니다.

저작권법에 따른 이용자의 권리는 위의 내용에 의하여 영향을 받지 않습니다.

이것은 [이용허락규약\(Legal Code\)](#)을 이해하기 쉽게 요약한 것입니다.

[Disclaimer](#)

공학박사학위논문

저임계, 임계, 초임계 영역에서의
원형 실린더 주위 유동: 비정상 유동
특성과 항력 모델링

Flow over a circular cylinder in the
subcritical, critical and super-critical
regimes: unsteady flow characteristics and
drag modeling

2022 년 2 월

서울대학교 대학원

기계항공공학부

진도현

공학박사학위논문

저임계, 임계, 초임계 영역에서의
원형 실린더 주위 유동: 비정상 유동
특성과 항력 모델링

Flow over a circular cylinder in the
subcritical, critical and super-critical
regimes: unsteady flow characteristics and
drag modeling

2022 년 2 월

서울대학교 대학원

기계항공공학부

진도현

저임계, 임계, 초임계 영역에서의 원형 실린더 주위유동: 비정상유동특성과항력모델링

Flow over a circular cylinder in the subcritical,
critical and super-critical regimes: unsteady flow
characteristics and drag modeling

지도교수 최 해 천

이 논문을 공학박사 학위논문으로 제출함

2021년 10월

서울대학교 대학원

기계항공공학부

진 도 현

진도현의 공학박사 학위논문을 인준함

2021년 12월

위 원 장 : 송 성 진

부위원장 : 최 해 천

위 원 : 황 원 태

위 원 : 손 기 현

위 원 : 김 도 균

Flow over a circular cylinder in the subcritical, critical and super-critical regimes: unsteady flow characteristics and drag modeling

Dohyun Jin

Department of Mechanical & Aerospace Engineering
Seoul National University

Abstract

Numerical simulations of the flows over a circular cylinder are conducted to investigate the unsteady flow characteristics and to propose predictive models of the drag coefficient.

In part I, we conduct large eddy simulations of flows around a circular cylinder in the subcritical, critical and super-critical regimes using an immersed boundary method. The Reynolds numbers considered in the study are 60000 for the subcritical regime, 250000 and 380000 for the critical regime and 850000 for the super-critical regime. The drag coefficients and the Strouhal numbers of the present simulation agree well with those of previous studies. At the subcritical regime, the favorable gradient of the mean surface pressure is observed after the separation point. Strong Karman vortex is developed close to the cylinder surface and the minimum pressure of the phase-averaged flow field is observed in the center of the Karman vortex. On the other hand, wide regions of pressure recovery along the cylinder surface are observed after the flow separation at the

critical and the super-critical regimes. The phase-averaged pressures in the Karman vortices at the regimes are higher than the pressure at the subcritical regime. The frequency of the shear layer vortex increases as the Reynolds number increases and the frequency normalized with the external azimuthal velocity and the momentum thickness at the laminar separation point is almost constant regardless of the Reynolds numbers at the critical and the super-critical regimes.

In part II, we suggest a predictive model of the drag coefficient of a circular cylinder using the information of the mean streamwise velocity and Reynolds normal stresses at a streamwise location in the wake. The boundary layer approximation in the wake and the Bernoulli equation in the inviscid region are used to model the contribution from the pressure distribution at the streamwise measurement location. To examine the accuracy of the present model, unsteady three-dimensional numerical simulations are conducted at various Reynolds numbers from laminar to super-critical regimes. The drag coefficients predicted from the present model agree very well with those from the present numerical simulation at the streamwise location downstream of the vortex formation region. We also revisit the universal Strouhal number concept and suggest new characteristic scales for the Karman vortex formation based on the mean streamwise velocity deficit at the centerline and the half-width of the wake. Using the characteristic scales at the streamwise location where the mean velocity deficit divided by the half-width becomes maximum, we propose another predictive model of the drag coefficient of a circular cylinder. With additional assumptions validated by the present simulation results, we propose a scaling law describing the relation among the drag coefficient, the Strouhal number and the base pressure coefficient.

Available data not only for a circular cylinder but also for other two-dimensional bluff bodies are applied to the present scaling law, showing excellent collapses onto the scaling law.

Keywords: circular cylinder, wake, Karman vortex, scaling law, drag model

Student number: 2013-22501

Contents

| | |
|---|------------|
| Abstract | i |
| Contents | iv |
| List of Figures | vi |
| List of Tables | xii |
| | |
| Part I A numerical study of flows over a circular cylinder in the subcritical, critical and super-critical regimes | 1 |
| | |
| 1 Introduction | 2 |
| | |
| 2 Numerical methods | 7 |
| 2.1. Governing equations and computational details | 7 |
| 2.2. Validation | 9 |
| | |
| 3 Results and discussions | 19 |
| 3.1. Mean flow characteristics | 19 |
| 3.2. Periodic flow characteristics during the Karman vortex formation | 22 |

| | |
|---|------------|
| 3.3. Unsteady flow characteristics of the separated shear layer | 24 |
| 4 Conclusions | 50 |
| | |
| Part II Universal relations between the drag and the wake of a circular cylinder | 52 |
| | |
| 1 Introduction | 53 |
| | |
| 2 Numerical methods | 58 |
| 2.1. Simulation cases | 58 |
| 2.2. Validation | 59 |
| | |
| 3 A predictive model of the drag coefficient based on the velocity information in the wake | 62 |
| 3.1. Formulation for the drag coefficient model | 62 |
| 3.2. Validity of the assumptions | 67 |
| 3.3. Criteria for the accurate prediction | 71 |
| | |
| 4 Universal Strouhal number and a scaling law regarding the drag | 80 |
| 4.1. Characteristic scales for the vortex formation | 80 |
| 4.2. A scaling law for the drag of two-dimensional bluff bodies | 83 |
| | |
| 5 Conclusions | 98 |
| | |
| References | 100 |
| | |
| Abstract (in Korean) | 107 |

List of Figures

Part I A numerical study of flows over a circular cylinder in the subcritical, critical and super-critical regimes

| | | |
|-----|---|----|
| 1.1 | Base pressure coefficient vs. Re from Williamson (1996). | 6 |
| 2.1 | Schematic diagram of the coordinates, computational domain and boundary conditions. | 14 |
| 2.2 | Comparison with literature: (a) the drag coefficients (C_D); (b) the Strouhal numbers ($St = fd/u_\infty$). \bullet , present; \square , Schewe (1983); \triangleright , Cadot <i>et al.</i> (2015); \diamond , MARIN experiment from Vaz <i>et al.</i> (2007); ∇ , Bearman (1969); \triangleleft , Achenbach & Heinecke (1981); \blacktriangledown , Ibrahim <i>et al.</i> (2016); \blacktriangle , Mousaied <i>et al.</i> (2014); \bullet , Rodríguez <i>et al.</i> (2015); \bullet , Yeon <i>et al.</i> (2016); \bullet , Cheng <i>et al.</i> (2017). | 15 |
| 2.3 | Separation angles. \bullet , present; \square , Adachi (1995); \triangleright , Capone <i>et al.</i> (2016); ∇ , Achenbach (1968); \triangleleft , Norberg (2003); \bullet , Rodríguez <i>et al.</i> (2015); \bullet , Yeon <i>et al.</i> (2016); \bullet , Cheng <i>et al.</i> (2017). | 16 |

| | | |
|-----|--|----|
| 2.4 | Surface pressure coefficient: (a) $Re = 60000$; (b) 250000 ; (c) 380000 ; (d) 850000 | 17 |
| 2.5 | Grid resolution near the cylinder surface (at 45° , near pres- sure minimum and separation point): (a) $Re = 60000$; (b) 250000 ; (c) 380000 ; (d) 850000 . Red circle symbols rep- resent the location where the velocity for the azimuthal direction is the maximum. | 18 |
| 3.1 | Surface pressure coefficients along the azimuthal direction. The separation point is shown with X symbols. \bullet , $Re =$ 60000 ; \bullet , $Re = 250000$; \bullet , $Re = 380000$; \bullet , $Re = 850000$. . | 27 |
| 3.2 | Mean streamlines: (a) $Re = 60000$; (b) 250000 ; (c) 380000 ; (d) 850000 | 28 |
| 3.3 | Mean pressure coefficients: (a) $Re = 60000$; (b) 250000 ; (c) 380000 ; (d) 850000 | 29 |
| 3.4 | Mean spanwise vorticity: (a) $Re = 60000$; (b) 250000 ; (c) 380000 ; (d) 850000 | 30 |
| 3.5 | Reynolds normal stresses in streamwise direction: (a) $Re =$ 60000 ; (b) 250000 ; (c) 380000 ; (d) 850000 | 31 |
| 3.6 | Reynolds normal stresses in transverse direction: (a) $Re =$ 60000 ; (b) 250000 ; (c) 380000 ; (d) 850000 | 32 |
| 3.7 | Reynolds normal stresses in spanswise direction: (a) $Re =$ 60000 ; (b) 250000 ; (c) 380000 ; (d) 850000 | 33 |
| 3.8 | Reynolds shear stresses: (a) $Re = 60000$; (b) 250000 ; (c) 380000 ; (d) 850000 | 34 |
| 3.9 | Turbulent kinetic energy: (a) $Re = 60000$; (b) 250000 ; (c) 380000 ; (d) 850000 | 35 |

| | | |
|------|---|----|
| 3.10 | Definition for each phase from the time signal of the lift coefficients at $Re = 250000$ | 36 |
| 3.11 | Phase-averaged pressure coefficients at $Re = 60000$: (a) 0 ($C_{L,max}$); (b) $\pi/5$; (c) $2\pi/5$; (d) $3\pi/5$ | 37 |
| 3.12 | Phase-averaged spanwise vorticity contours at $Re = 60000$: (a) 0 ($C_{L,max}$); (b) $\pi/5$; (c) $2\pi/5$; (d) $3\pi/5$ | 38 |
| 3.13 | Phase-averaged pressure coefficients at $Re = 250000$: (a) 0 ($C_{L,max}$); (b) $\pi/5$; (c) $2\pi/5$; (d) $3\pi/5$ | 39 |
| 3.14 | Phase-averaged spanwise vorticity contours at $Re = 250000$: (a) 0 ($C_{L,max}$); (b) $\pi/5$; (c) $2\pi/5$; (d) $3\pi/5$ | 40 |
| 3.15 | Phase-averaged pressure coefficients at $Re = 380000$: (a) 0 ($C_{L,max}$); (b) $\pi/5$; (c) $2\pi/5$; (d) $3\pi/5$ | 41 |
| 3.16 | Phase-averaged spanwise vorticity contours at $Re = 380000$: (a) 0 ($C_{L,max}$); (b) $\pi/5$; (c) $2\pi/5$; (d) $3\pi/5$ | 42 |
| 3.17 | Phase-averaged pressure coefficients at $Re = 850000$: (a) 0 ($C_{L,max}$); (b) $\pi/5$; (c) $2\pi/5$; (d) $3\pi/5$ | 43 |
| 3.18 | Phase-averaged spanwise vorticity contours at $Re = 850000$: (a) 0 ($C_{L,max}$); (b) $\pi/5$; (c) $2\pi/5$; (d) $3\pi/5$ | 44 |
| 3.19 | Angular fluctuation during Karman vortex shedding obtained from the phase-averaged flow fields: (a) separation point; (b) stagnation point. | 45 |
| 3.20 | Instantaneous spanwise vorticity contours: (a) $Re = 60000$; (b) 250000 ; (c) 380000 ; (d) 850000 | 46 |
| 3.21 | Power spectral density at the separated shear layer: (a) $Re = 60000$, $x/d = 0.096$, $y/d = 0.542$; (b) $Re = 250000$, $x/d = 0.096$, $y/d = 0.542$; (c) $Re = 380000$, $x/d = 0.133$, $y/d = 0.497$; (d) $Re = 850000$, $x/d = 0.174$, $y/d = 0.479$ | 47 |

| | | |
|------|--|----|
| 3.22 | Frequencies of the shear layer vortices and the Karman vortices: (a) the Strouhal number (fd/u_∞); (b) frequency ratio (f_{SL}/f_{KV}). \circ , shear layer vortex; \diamond , Karman vortex; \diamond Prasad & Williamson (1997); \square , Norberg (1987); \triangleright , Wei & Smith (1986); \triangleleft , Bloor (1964); \triangle , Okamoto <i>et al.</i> (1981); \square , Mihailovic & Corke (1997); \triangle , Ahmed & Wagner (2003). | 48 |
| 3.23 | The shear layer frequency normalized by the momentum thickness and the external azimuthal velocity at the separation point. | 49 |

Part II Universal relations between the drag and the wake of a circular cylinder

| | | |
|-----|---|----|
| 2.1 | Variations of the drag coefficient and Strouhal number with the Reynolds number: (a) C_D vs. Re ; (b) St vs. Re . Present (red circle), Wieselsberger (1922) (∇), Roshko (1954) (\triangleleft), Achenbach & Heinecke (1981) (\triangle), Schewe (1983) (\diamond), Williamson (1992) (\triangleright), Kim & Choi (2005) (\circ), Cadot <i>et al.</i> (2015) (\square). | 61 |
| 3.1 | Schematic diagram of the control volume analysis. | 74 |

| | | |
|-----|--|----|
| 3.2 | Contribution to C_D from each term in (3.18): with integration range equal to the domain size; (a) $Re = 50$; (b) 3900; (c) 250000; at $x/d = 5$; (d) $Re = 50$; (e) 3900; (f) 250000; at $x/d = 10$ (g) $Re = 50$; (h) 3900; (i) 250000. Black dashed line, C_D ; black solid line, contribution from convective flux at the outlet; blue solid line, contribution from the pressure at the outlet; green solid line, contribution from the viscous diffusion at the outlet; red dashed line, contribution from the pressure and the viscous diffusion at the streamline. | 75 |
| 3.3 | Pressure coefficients (C_p) and effects of the pressure coefficient estimation ($C_p + 2\overline{v'^2}/u_\infty^2$): (a) $Re = 50$; (b) 3900; (c) 250000. Total pressure coefficients (C_{P_t}): (d) $Re = 50$; (e) 3900; (f) 250000. The mean streamwise velocity deficits ($1 - \bar{u}/u_\infty$): (g) $Re = 50$; (h) 3900; (i) 250000. Black line, $x/d = 5$; blue line, $x/d = 7.5$; red line, $x/d = 10$. In (a), (b) and (c), solid line, $C_p + 2\overline{v'^2}/u_\infty^2$; dashed line, C_p . . . | 76 |
| 3.4 | Measured and predicted drag coefficients at $x/d = 10$. \blacklozenge , $C_{D,CFD}$; \circ , present; \triangle , Dimotakis (1977); \square , Antonia & Rajagopalan (1990). | 77 |
| 3.5 | Variations of the drag coefficient predicted by the present model with x_m ($H = L_y$): (a) $C_D/C_{D,CFD}$ vs. x_m/d ; (b) $C_D/C_{D,CFD}$ vs. $(x_m - x_{vm})/y_{1/2}$ | 78 |
| 3.6 | Variations of the drag coefficient predicted by the present model with H ($(x_m - x_{vm})/y_{1/2} = 10$): (a) $C_D/C_{D,CFD}$ vs. H/d ; (b) $C_D/C_{D,CFD}$ vs. $H/y_{1/2}$ | 79 |

| | | |
|------|---|----|
| 4.1 | Comparison for characteristic velocity scales. | 88 |
| 4.2 | Wake coordinate statistics along the centerline at $Re = 3900$: (a) half width ($y_{1/2}/d$); (b) mean velocity deficit . . | 89 |
| 4.3 | Comparison of the universal Strouhal numbers. | 90 |
| 4.4 | Streamwise location for the vortex formation origin: (a) present suggestion; (b) present suggestion compared with other studies. | 91 |
| 4.5 | Budget analysis for the drag coefficient at $x = x_{dm}$ for $Re = 3900$: (a) conventional formulation; (b) velocity deficit and total pressure based formulation. Red line, mean velocity; blue line, Reynolds stress; green line, pressure (static or total); black line, sum of the budgets; dashed line, $C_{D,CFD}$ | 92 |
| 4.6 | (a) Comparison between $\alpha_{theory} \frac{\bar{u}_{dc}^2}{u_\infty^2} \frac{y_{1/2}}{d}$ and $\frac{1}{d} \int_{-\frac{H}{2}}^{\frac{H}{2}} -\frac{\bar{u}_{dc}^2}{u_\infty^2} dy$; (b) measured α | 93 |
| 4.7 | $C_D + \frac{1}{d} \int_{-\frac{H}{2}}^{\frac{H}{2}} -\frac{\bar{u}_{dc}^2}{u_\infty^2} dy$ versus $C_{p_{tc}} \frac{y_{1/2}}{d}$ | 94 |
| 4.8 | C_D from the simulation versus C_D from modeling based on the characteristic scales at x_{dm} | 95 |
| 4.9 | (a) \bar{u}_{dc}/u_∞ versus Re ; (b) $-C_{p_{tc}}$ versus $1 - C_{pb}$ at x_{dm} | 96 |
| 4.10 | The performance of the scaling law regarding C_D, St and C_{pb} : (a) C_D versus $(0.22 - C_{pb})/St$; (b) C_D and $C_D St / (0.22 - C_{pb})$ depending on the Re . Solid and open symbols represent C_D and $C_D St / (0.22 - C_{pb})$, respectively and \circ , present; \diamond , flat plate at $Re = 3000$, \square , square prism at $Re = 22000$ (Cao <i>et al.</i> 2020) \triangleleft , boat-tailed bluff body at $Re = 96000$ (Mariotti <i>et al.</i> 2019). | 97 |

List of Tables

Part I A numerical study of flows over a circular cylinder in the subcritical, critical and super-critical regimes

| | | |
|-----|-------------------------------------|----|
| 2.1 | Summary of the simulations. | 13 |
|-----|-------------------------------------|----|

Part II Universal relations between the drag and the wake of a circular cylinder

| | | |
|-----|-------------------------------------|----|
| 2.1 | Summary of the simulations. | 60 |
|-----|-------------------------------------|----|

Part I.

A numerical study of flows over a circular
cylinder in the subcritical, critical and
super-critical regimes

Chapter 1

Introduction

The circular cylinder is a representative shape of the two-dimensional bluff body and has attracted engineering attention in a wide range of fields such as wind turbine towers, bridge piers and marine structures. The geometry of a circular cylinder is simple but the the flow phenomena around the cylinder are quite complex so that various researches have been conducted. The main parameter that determines the characteristics of the flow around the circular cylinder is the Reynolds number (Re). The flow is steady at the low Reynolds numbers. As the Reynolds number increases, the flow changes from steady state to unsteady state and becomes three-dimensional flow. Figure 1.1 shows the negative value of the base pressure coefficient depending on the Reynolds number from Williamson (1996). The base pressure changes in various ways for each flow regime. In particular, when the Reynolds number reaches about 200000, there is a regime where the base pressure changes abruptly, which is known as critical regime. A regime that maintains relatively large value before that is defined as subcritical regime, and a regime that maintains almost

constant value after the change is defined as super-critical regime.

A substantial decrease of the drag coefficient (C_D) and the RMS lift coefficient ($C_{L,rms}$), and the increase of the Strouhal number (St) have been also observed for the critical regime. In particular, the rapid drop of the drag coefficient is referred as the drag crisis. These changes between regimes are related to the change of the location where the transition to turbulence phenomenon occurs. In the subcritical regime, the flow is separated from the laminar boundary layer and transition to turbulent flow occurs from the separated shear layer, whereas in the super-critical regime, the flow separation also occurs from the laminar boundary but turbulent reattachment occurs so that main flow separation is delayed. Separation bubbles are symmetrically formed on the top and bottom of the cylinder in the super-critical regime. In the critical regime, transition to super-critical regime occurs and the delay of the boundary layer separation has been observed but the detailed physics after the flow separation is not clear. Also, irregular or asymmetric transition phenomena have been observed.

Previous experimental studies have been measured forces acting on the cylinder and Karman vortex shedding frequency during drag crisis. Achenbach (1968) measured the distribution of the surface pressure and skin friction distribution around a circular cylinder for $60000 < Re < 5000000$. They commented that the effects of the pressure gradient on the boundary layer of the cylinder was non-negligible so that there was great uncertainty in measuring the skin friction coefficient in turbulent boundary layers. Bearman (1969) measured not only the force coefficient but also the time trace of the velocity in the wake for $100000 < Re < 750000$. He observed the discontinuous increase in the Strouhal number in the

critical regime and related this phenomena with asymmetric transition in the upper and the lower surface boundary layer. Schewe (1983) also conducted force measurements from the subcritical to transcritical Reynolds numbers ($23000 < Re < 7100000$) and observed non-zero mean lift in the critical regime. He also observed that the transitions were coupled with a drop of the C_D and a jump of the St and observed hysteresis. Since then, asymmetric mean flow was regarded as the fundamental physics of a circular cylinder boundary layer transition. However, Cadot *et al.* (2015) observed the symmetric transition as well as the asymmetric transition. They concluded that the asymmetric states are not the only route for the turbulent reattachment during the drag crisis and the symmetric scenario is possible. They suggested that the full understanding of this scenario needs the investigation of the reattachment dynamics during drag crisis. Although many experimental studies have been conducted on the wake topology and local pressure distribution, only a few studies have been conducted on the coherent structures for transition to turbulence. Pfeil & Orth (1990) investigated the laminar separation bubble dynamics with and without the inflow disturbances but their experiments were conducted on the cylinder with the splitter plate installed at the rear side of the cylinder.

Most of the numerical analysis have been conducted at the Reynolds number less than 10000 due to the limits of computing resources (Dong & Karniadakis 2005), which is a much less than the Reynolds number for the drag crisis. In particular, many researches, including (Beaudan & Moin 1994; Kravchenko & Moin 2000), have been conducted on the flow of circular cylinders by adopting large eddy simulations at $Re = 3900$. Recently, few studies have been conducted on the flow from the critical to

the supercritical regime adopting large eddy simulation (LES) (Rodríguez *et al.* 2015; Yeon *et al.* 2016; Cheng *et al.* 2017). Rodríguez *et al.* (2015) analyzed the topology of the wake, the instantaneous characteristics of drag and lift, and the frequency characteristics. Yeon *et al.* (2016) conducted verification studies investigating the effects of grid resolution, aspect ratio and convection scheme. They observed that the grid uncertainties were quite large and the aspect ratio should be small to simulate critical and super-critical Reynolds numbers. Cheng *et al.* (2017) studied the change of the surface friction depending on the Reynolds number. Although many studies have been conducted for these regimes, the detailed dynamics of the unsteady flows over a circular cylinder are not fully understood.

The objectives of the present study are to investigate unsteady characteristics of the flows over a circular cylinder such as separating shear layer, transitional separation bubble and Karman vortices. We conduct LES of the flows over a circular cylinder in the subcritical, critical and supercritical regimes. A further insight into the characteristics of the flows during the drag crisis is presented by analyzing the coherent structures in the separated shear layer and the wake using mean, phase-averaged and instantaneous flow fields.

This part is organized as follows. The numerical methods used in this study are described in Chapter 2. The characteristics of flow around a circular cylinder are discussed in Chapter 3. Finally, summary and conclusion is followed in Chapter 4.

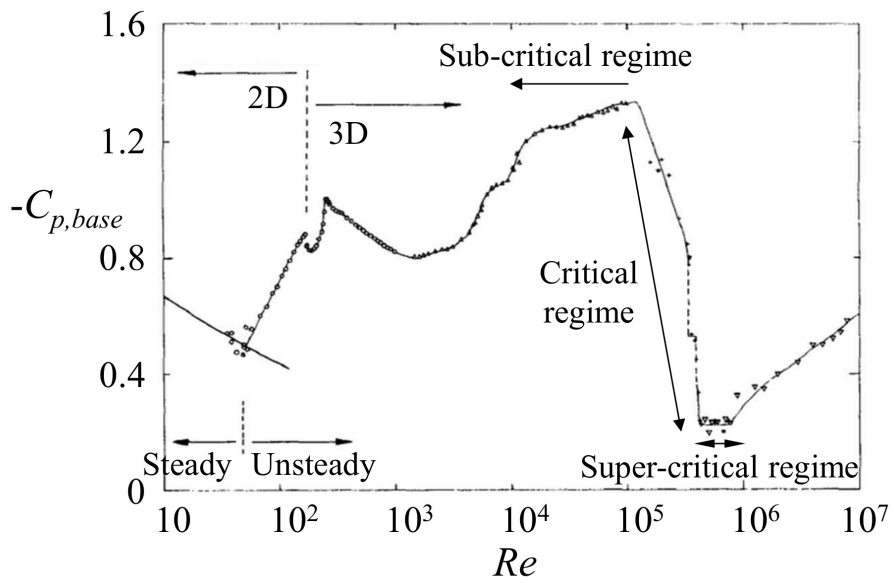


FIGURE 1.1. Base pressure coefficient vs. Re from Williamson (1996).

Chapter 2

Numerical methods

2.1. Governing equations and computational details

The governing equations of the unsteady incompressible viscous flow for large eddy simulation (LES) are filtered continuity and incompressible Navier-Stokes equations:

$$\frac{\partial \tilde{u}_i}{\partial x_i} - q = 0, \quad (2.1)$$

$$\frac{\partial \tilde{u}_i}{\partial t} + \frac{\partial \tilde{u}_i \tilde{u}_j}{\partial x_j} = -\frac{\partial \tilde{p}}{\partial x_i} + \frac{1}{Re} \frac{\partial^2 \tilde{u}_i}{\partial x_j \partial x_j} - \frac{\partial \tau_{ij}}{\partial x_j} + f_i, \quad (2.2)$$

where t is time, $x_i=(x, y, z)$ are the Cartesian coordinates (streamwise, transverse and spanwise directions, respectively), $u_i=(u, v, w)$ are the corresponding velocity components, p is the pressure and overtilde denotes the filtering operation for LES. The Reynolds number is defined as $Re = u_\infty d/\nu$, where u_∞ , d and ν denote the free-stream velocity, the cylinder diameter and kinematic viscosity, respectively. An immersed boundary method (Kim *et al.* 2001) is used to satisfy the no-slip condition at the cylinder surface, and q and f_i denote the mass source/sink and the momentum forcing, respectively. $\tau_{ij} = \widetilde{u_i u_j} - \tilde{u}_i \tilde{u}_j$ is the subgrid-scale (SGS) stress tensor and a dynamic global eddy viscosity model (Park

et al. 2006; Lee *et al.* 2010) is used to determine the SGS stress tensor. A finite volume method in a staggered Cartesian grid system is used for the governing equations. A fully-implicit fractional step method by Choi & Moin (1994) is adopted to decouple the continuity and the momentum equations with linearization proposed by Kim *et al.* (2002). The Crank-Nicolson method is implemented for the time integration and the 2nd order central difference scheme is used for the spatial discretization. We adopted message passing interface (MPI) for the parallelization.

Figure 2.1 represents the numerical domain and boundary conditions for each side of the domain. The Dirichlet condition is used at the inlet with a uniform velocity profile ($u = u_\infty, v = w = 0$). On the top and bottom boundaries, $\partial u / \partial y = v = \partial w / \partial y = 0$ is applied. At the exit, a convective boundary condition is adopted as $\partial u_i / \partial t + u_c \partial u / \partial x = 0$, where u_c is the streamwise velocity averaged at the outlet plane. The periodic boundary condition is adopted for the spanwise direction. The size of computational time step is obtained from maximum Courant-Friedrichs-Lewy (CFL) number condition, $CFL = \Delta t (|u| / \Delta x + |v| / \Delta y + |w| / \Delta z) \leq 1.5$.

The Reynolds numbers used in the present study are shown in table 2.1 with simulation method (DNS/LES), computational domain sizes and the numbers of grids. L_x, L_y and L_z represent the size of the computation domain in streamwise, transverse and spanwise direction, respectively. N_x, N_y and N_z represent the number of grids in streamwise, transverse and spanwise direction, respectively. We simulate flows corresponding to the Reynolds number 60000 for the subcritical regime, 250000 and 380000 for the critical regime, and 850000 for the super-critical regime.

2.2. Validation

Although researches found the similar tendency of drag forces, it is hard to measure the exact value at each Reynolds number. Figure 2.2(a) shows the drag coefficients from the present simulation with those from the previous studies (Schewe 1983; Vaz *et al.* 2007; Cadot *et al.* 2015; Ibrahim *et al.* 2016; Moussaed *et al.* 2014; Rodríguez *et al.* 2015; Yeon *et al.* 2016; Cheng *et al.* 2017). The drag crisis is observed in the critical regime. After drag crisis, almost constant drag is observed in the super-critical regime. Note that this tendency can also be observed in three-dimensional body such as golf ball. The results from the experiments are shown with open symbols in figure 2.2. Even for the sub-critical regime, about 20% differences can be observed among experiments. Conducting experiment in high Reynolds number is very challenging since the physics in these regimes are very sensitive to small disturbances and the limitation of apparatus. Blockage ratio and aspect ratio of most studies have been conducted within 10 except the study from Cadot *et al.* (2015). Free-stream turbulence may also affect the results.

Figure 2.2(b) shows the Strouhal number versus Reynolds number from the present simulation with those from the previous studies (Schewe 1983; Achenbach & Heinecke 1981; Bearman 1969; Ibrahim *et al.* 2016; Moussaed *et al.* 2014; Rodríguez *et al.* 2015; Yeon *et al.* 2016; Cheng *et al.* 2017). The drag crisis is clearly observed in the critical regime. After the drag crisis, almost constant drag is observed in the super-critical regime. Note that this tendency can also be observed in a three-dimensional body such as golf ball. The Strouhal number remains almost constant value of 0.2 in the subcritical regime. It increases in the critical regime, and the Strouhal number in the super-critical regime is much higher than that in

the subcritical regime.

The highest Reynolds number simulated using direct numerical simulation is only 10000 which is much lower than the Reynolds numbers correspond to critical regime. Therefore, simulations with modeling have been conducted for the high Reynolds number flows. Simulations using RANS models have obtained relatively inaccurate results at some Reynolds numbers as shown in figure 2.2. Recently, a few studies have been conducted using large eddy simulations. As you can see, they showed promising results for predicting high Reynolds number flows. Although, even in numerical results the values between researches are quite different, LES is a suitable comprise to investigate the complex flow structures at high Reynolds numbers between the cost and the accuracy. Within these differences, the results from the present simulation agree well with previous studies. The drag crisis and the increase of the Strouhal number are reproduced well from the present simulation.

Figure 2.3 shows the mean separation angles compared with previous studies (Adachi 1995; Capone *et al.* 2016; Norberg 2003; Achenbach 1968; Rodríguez *et al.* 2015; Yeon *et al.* 2016; Cheng *et al.* 2017). For the subcritical regime, the variation between experiments are quite large. For example, the angles from Adachi (1995) are about 100° while those from Norberg (2003); Capone *et al.* (2016) are less than 80° . The reason for this discrepancy might be related to experimental apparatus for measuring the angle and the strong interaction between the Karman vortex and the separation angle (or the angle change during vortex shedding). The detailed analysis will be discussed in chapter 3. For the critical Reynolds numbers, the separation angle increases as the Reynolds number increases. For the super-critical Reynolds number, the separation

angle is largely delayed. Note that Achenbach (1968) commented about their measurement method might have large uncertainty for the super-critical Reynolds number since their method have not been calibrated for the turbulent boundary layer flow. Quite large variations of the separation angles (about 20°) are observed not only from the experimental results (Achenbach 1968; Adachi 1995) but also from the LES simulation results (Rodríguez *et al.* 2015; Cheng *et al.* 2017). The present simulation successfully captures the turbulent boundary layer separation in the super-critical Reynolds number within the LES simulation results from Rodríguez *et al.* (2015); Cheng *et al.* (2017).

The surface pressure coefficients at $Re = 60000, 250000, 380000$ and 850000 are also compared with previous researches (Cheng *et al.* 2017; Lehmkuhl *et al.* 2014; Rodríguez *et al.* 2015; Weidman 1968; Cantwell & Coles 1983; Farell & Blessmann 1983; Achenbach 1968) to check the validity of the present LES results (figure 2.4). At the upper subcritical regime ($Re = 60000$), the Reynolds number effect on the force coefficient is small so that the pressure distribution agree well with each other regardless of the Reynolds numbers. At the critical regime, since the drag coefficient decreases with the Reynolds number, the pressure coefficient distribution is sensitive to the Reynolds number and might be different from each study. Nonetheless, the pressure distribution from the present simulation is in quite a good agreement with that of previous studies. The minimum pressure and the base pressure are within the experimental results (see figure 2.3b-c). At $Re = 850000$, the pressure distributions of the present simulation and Rodríguez *et al.* (2015) are quite similar, while the base pressures of Cheng *et al.* (2017) and Achenbach (1968) are similar but the angles at the pressure minimum are quite different. Although we

cannot conclude that which one is more accurate, the present simulation results are consistent with the well-known tendencies during the drag crisis. The base pressure coefficient from Cheng *et al.* (2017) at $Re = 380000$ is higher than that at $Re = 850000$ which disagrees with the base pressure changes from Williamson (1996). Also, the base pressure from Lehmkuhl *et al.* (2014) is lower than that from Farell & Blessmann (1983) even though the minimum pressure from Lehmkuhl *et al.* (2014) is lower than that from Farell & Blessmann (1983). In the critical regime, the minimum pressure decreases and the base pressure increases. The present results in figure 2.4(b-c) lie within the experimental studies, showing the adequacy of the present numerical setup.

The grid resolution near the cylinder surface in the present study is shown in figure 2.5. At 45° in azimuthal direction, the number of grids inside the boundary layer is approximately 6. The edge of the boundary layer is obtained from the location where the velocity in azimuthal direction is the maximum. Since the thickness of the boundary layer increases along the azimuthal direction before the flow separation, the number of grids inside the boundary layer increases.

| Re | DNS/LES | L_x/d | L_y/d | L_z/d | N_x | N_y | N_z |
|--------|---------|---------|---------|----------|-------|-------|-------|
| 60000 | LES | 30 | 50 | π | 1025 | 641 | 80 |
| 250000 | LES | 24 | 50 | 0.5π | 1793 | 1025 | 128 |
| 380000 | LES | 24 | 50 | 0.5π | 2048 | 1169 | 128 |
| 850000 | LES | 20 | 30 | 0.5 | 3585 | 2369 | 64 |

TABLE 2.1. Summary of the simulations.

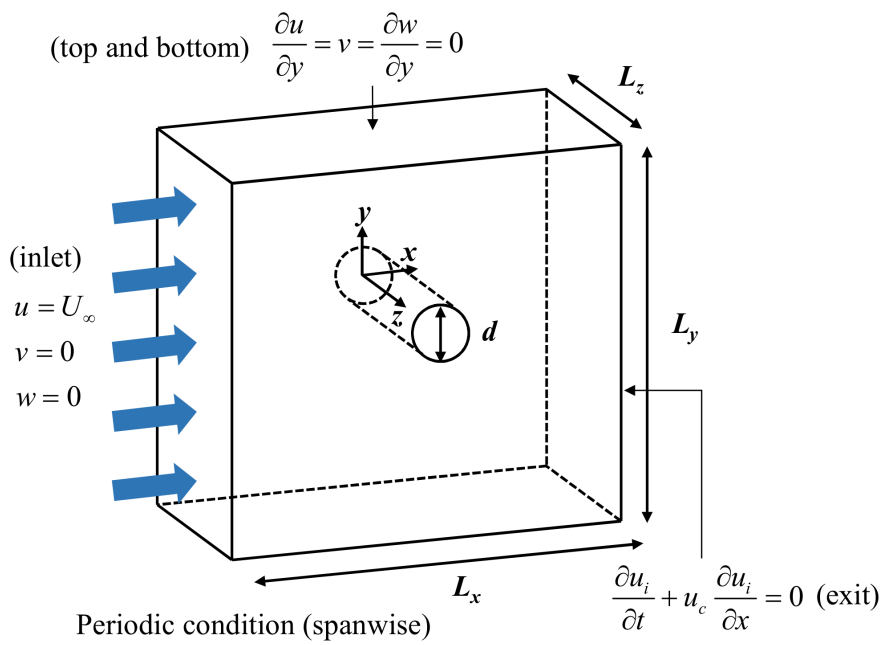


FIGURE 2.1. Schematic diagram of the coordinates, computational domain and boundary conditions.

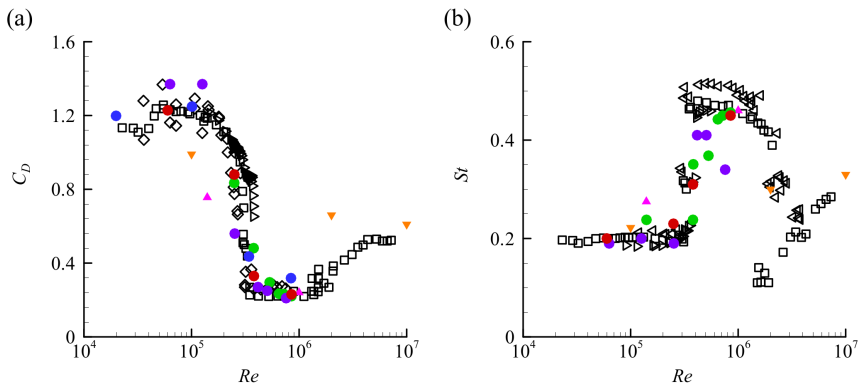


FIGURE 2.2. Comparison with literature: (a) the drag coefficients (C_D); (b) the Strouhal numbers ($St = fd/u_\infty$). \bullet , present; \square , Schewe (1983); \triangleright , Cadot *et al.* (2015); \diamond , MARIN experiment from Vaz *et al.* (2007); ∇ , Bearman (1969); \triangleleft , Achenbach & Heinecke (1981); \blacktriangledown , Ibrahim *et al.* (2016); \blacktriangle , Moussaed *et al.* (2014); \bullet , Rodríguez *et al.* (2015); \bullet , Yeon *et al.* (2016); \bullet , Cheng *et al.* (2017).

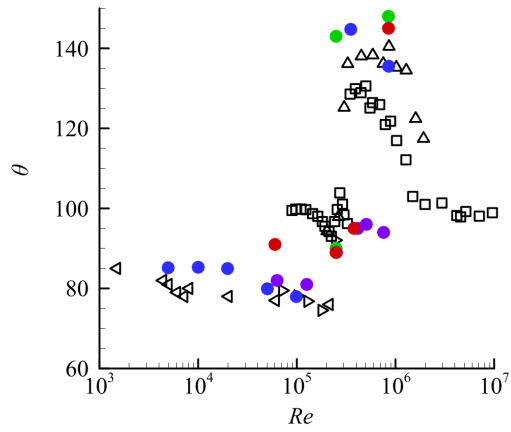


FIGURE 2.3. Separation angles. \bullet , present; \square , Adachi (1995); \triangleright , Capone *et al.* (2016); ∇ , Achenbach (1968); \triangleleft , Norberg (2003); \bullet , Rodríguez *et al.* (2015); \bullet , Yeon *et al.* (2016); \bullet , Cheng *et al.* (2017).

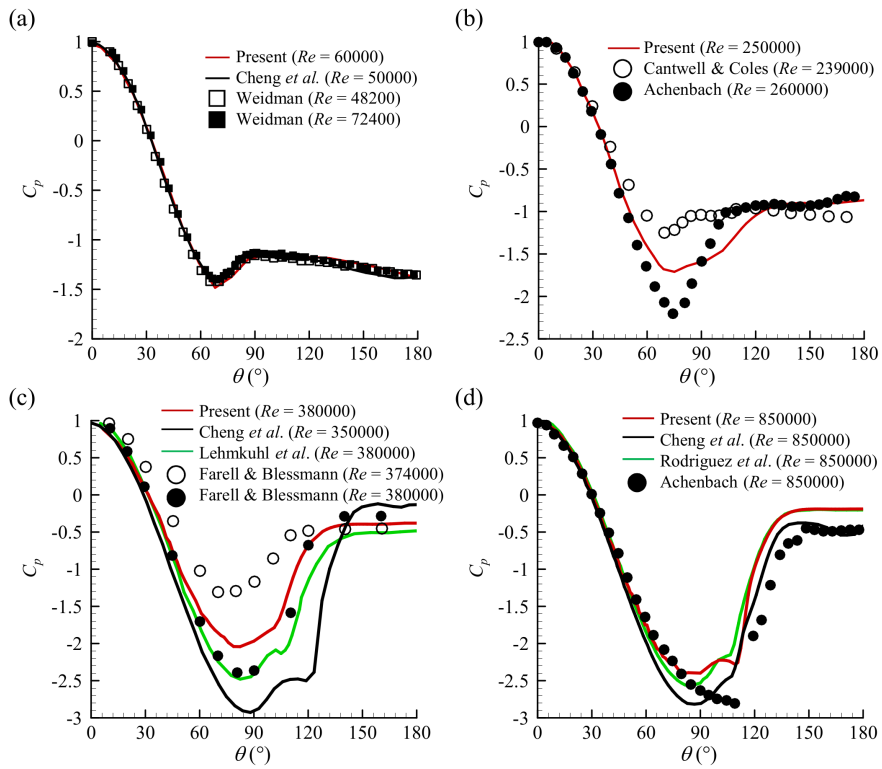


FIGURE 2.4. Surface pressure coefficient: (a) $Re = 60000$; (b) 250000 ; (c) 380000 ; (d) 850000 .

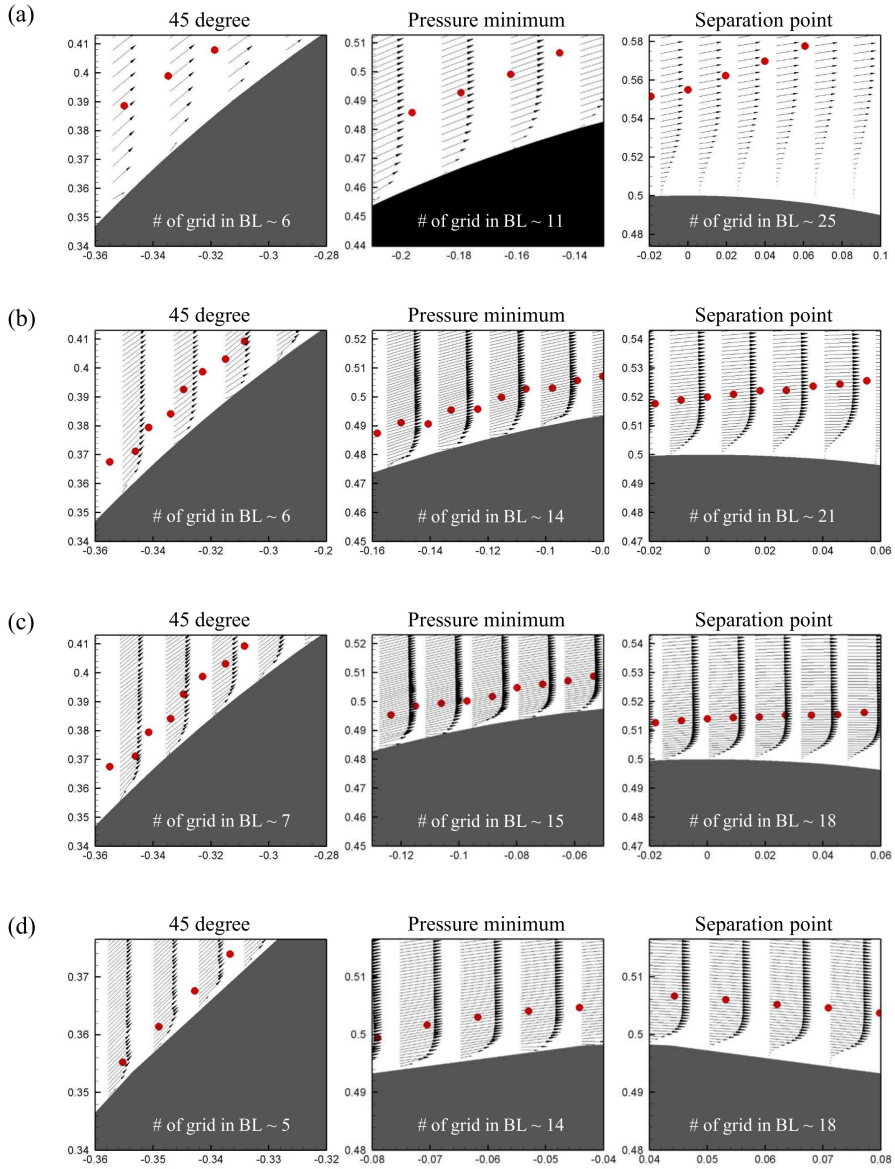


FIGURE 2.5. Grid resolution near the cylinder surface (at 45° , near pressure minimum and separation point): (a) $Re = 60000$; (b) 250000 ; (c) 380000 ; (d) 850000 . Red circle symbols represent the location where the velocity for the azimuthal direction is the maximum.

Chapter 3

Results and discussions

3.1. Mean flow characteristics

Figure 3.1 shows the mean pressure coefficients along the cylinder surface in the azimuthal direction. As the Reynolds number increases, the minimum pressure decreases and the base pressure increases. The minimum surface pressures are observed upstream of the laminar flow separation point regardless of the Reynolds number but the corresponding angle increases with the Reynolds number. In the sub-critical regime ($Re = 60000$), the surface pressure decreases after the flow separation. In the critical and the super-critical regimes, the wide region of surface pressure recovery is observed after the (laminar) flow separation point. The relevant flow characteristics will be analyzed in this chapter.

Figure 3.2 shows the mean streamlines near the cylinder. The width of the recirculation region in the present study is defined as the transverse distance between the upper and the lower core of the recirculation bubble and the length of the recirculation bubble is defined as x/d where $\bar{u} = 0$. The width of the recirculation region decreases as the Reynolds number

increases. On the other hand, the length of the recirculation bubble is the longest at $Re = 380000$ and the shortest at $Re = 60000$ among the present simulation results.

Figure 3.3 shows the contours of the mean pressure coefficient. A contour interval is the same with 0.05 for all the cases. The mean pressure gradient inside the recirculation bubble at $Re = 60000$ is much larger than that at the other Reynolds numbers which seems to be closely related to the distribution of the surface pressure coefficient shown in figure 3.1. This phenomenon will be analyzed in the next section.

Figure 3.4 shows the contours of the mean spanwise vorticity. The separated shear layer becomes closer to the cylinder surface as the Reynolds number increases. At $x/d = 0.25$ which corresponds to $\theta = 120^\circ$ where a clear difference in the shear layer location is observed between the sub-critical and the other regimes, the centerline of the separated shear layer at $Re = 60000$ locates at $y/d > 0.5$, whereas that at the other Reynolds numbers locates at $y/d < 0.5$. The detailed physics will be analyzed in this chapter.

Not only the mean components but also the fluctuation components show clear differences among the regimes (figure 3.5-3.9). Figure 3.5 shows the contours of the Reynolds normal stress in the streamwise direction. The maximum Reynolds normal stress in the streamwise direction is observed at the separated shear layer regardless of the Reynolds number (figure 3.4 and 3.5). At $Re = 380000$ and 850000 , the local maximum is also observed in the wake behind the cylinder. Figure 3.6 shows the contours of the Reynolds normal stress in the transverse direction. The maximum Reynolds normal stress in the transverse direction is observed at a centerline location downstream of the cylinder at $Re = 60000, 250000$

and 380000. At $Re = 850000$, the maximum stress locates right above the cylinder surface and the location is very close to the location where the $\overline{u'^2}/u_\infty^2$ is maximum (figure 3.5(d)). Figure 3.7 shows the contours of the Reynolds normal stress in the spanwise direction. At $Re = 60000$, the maximum Reynolds normal stress in the spanwise direction is observed at a centerline location downstream of the cylinder and the location is very close to the cylinder base. At $Re = 250000$, 380000 and 850000, the maximum stress locates right above the cylinder surface. Figure 3.8 shows the contours of the Reynolds shear stress. The locally strong Reynolds shear stresses are observed in the wake region in $1 < x/d < 1.5$ regardless of the Reynolds number. However, at the critical and the super-critical Reynolds numbers, the maximum shear stresses are observed right above the cylinder surface in the separated shear layer. Figure 3.9 shows the contours of the turbulent kinetic energy. The maximum turbulent kinetic energy is observed at a centerline location downstream of the cylinder at $Re = 60000$, whereas that is observed in the separated shear layer right above the cylinder surface at the other Reynolds numbers.

To sum up, downstream from the laminar separation point, the wide region of the favorable surface pressure gradient is observed at the sub-critical Reynolds number, whereas the wide region of pressure recovery is observed at the critical and the super-critical Reynolds numbers. At the subcritical Reynolds number, the recirculation bubble is wide and inside the bubble strong pressure gradient is observed. The maximum Reynolds normal stress in the spanwise direction is observed at the centerline location very close to the cylinder base. At the critical and the super-critical Reynolds numbers, the separated shear layer right downstream of the mean separation point locates close to the cylinder surface and the tur-

bulent kinetic energy and the Reynolds shear stress are relatively large at the shear layer (compared to the wake region). It can be inferred from the mean statistics that the unsteady flow characteristics in the separated shear layer and the wake change a lot during the drag crisis.

3.2. Periodic flow characteristics during the Karman vortex formation

In this section, the characteristics of the unsteady flows related to the Karman vortex are discussed. Since the force coefficients are related to the formation and departure of large scale structures from the vortex formation region (Portela *et al.* 2018), the ensemble averaging is adopted by sampling the instantaneous flow fields based on the time signal of the lift coefficient. In order to improve statistical convergence, averaging in the spanwise direction is also conducted. We define each phase by dividing time interval equally between the maximum and minimum extreme values of the lift coefficients (see figure 3.10). The phase angle is discretized into 10 segments such that each time instant is associated with a phase $\phi = -\pi + n\frac{2\pi}{10}$, where $0 \leq n \leq 10$. The number of instantaneous fields used to obtain phase-averaged flow fields are as follows. 12, 10, 10 and 8 Karman vortex shedding cycles are used for $Re = 60000, 250000, 380000$ and 850000 , respectively.

Figure 3.11 and 3.12 show the phase-averaged pressure coefficients and the phase-averaged spanwise vorticity contours at $Re = 60000$. The minimum pressure is observed at the center of the vortex which locates right downstream of the cylinder surface. The location of the minimum pressure inside the Karman vortex becomes closer to the centerline right after the maximum lift phase (figure 3.11a). At the phase $2\pi/5$ (see figure

3.11c), the location of the minimum pressure is $x/d = 0.94$, $y/d = 0.07$. At the phase $3\pi/5$ (see figure 3.11d), the Karman vortex originated from the upper side locates away from the cylinder surface and the centerline compared to the phase $2\pi/5$. The phase-averaged base pressure is closely related to the transverse location of the minimum pressure inside the Karman vortex and the base pressure is always lower than the pressure on the other side of the cylinder surface. Therefore, the favorable surface pressure gradient at $Re = 60000$ (figure 3.1) might have a strong relationship with the Karman vortex formation process which occurs close to the surface. The location of the separated shear layer also changes during the Karman vortex formation process. When the lift is maximum, the shear layer at the upper side is located more close to the cylinder surface than that at the other side.

On the other hand, at the Reynolds numbers for the critical regimes, the pressure at the center of the Karman vortex is higher than the minimum pressure from the cylinder surface which is located upstream of the separation point (figure 3.13 and 3.15). Also, unlike the subcritical regime (figure 3.11), the low pressure region induced by the Karman vortex formation does not seem to affect the surface pressure distribution at $2\pi/5$ phase. From the vorticity fields in figure 3.14 and 3.16, non-negligible size of the vortical structures locates at the lower side right below the Karman vortex at the upper side when the lift is maximum.

At the super-critical regime, the pressure at the center of the Karman vortex is also higher than the minimum pressure from the cylinder the surface and the low pressure region induced by the Karman vortex formation does not seem to affect the surface pressure distribution at $2\pi/5$ phase (figure 3.17 and 3.18). From the vorticity field in figure 3.18, the

shape of the shedded Karman vortex can be approximated as an elliptic shape and the major axis seems to be much longer than the minor axis. The vortex shape at $Re = 850000$ is much more like that at the much lower Reynolds number such as 2d wake regime.

Figure 3.19 represents the amplitude of the fluctuations of the separation point and the stagnation point. As the Reynolds number increases, the amplitude of the fluctuations of the laminar separation point and the stagnation point decreases. Especially, for the subcritical regime, large fluctuations are observed even at the stagnation point.

3.3. Unsteady flow characteristics of the separated shear layer

Figure 3.20 shows the instantaneous vorticity contours near the separated shear layer. At $Re = 60000$, vortices are formed due to roll-up of the shear layer and the pairing of the shear layer vortices are observed. On the other hand, only the roll-up is observed for the critical and the super-critical Reynolds numbers.

Figure 3.21 shows the power spectral density for the transverse velocity. The peak frequencies which are lower than 1 are related to the Karman vortex and those larger than 1 represent the roll-ups of the shear layer and pairing of the shear layer vortices. At $Re = 60000$, two peaks are observed, and the frequency of a peak corresponds to shear layer roll-up is 9.0 and that corresponds to the vortex pairing is 4.6 (figure 3.21a). The frequencies of the peaks correspond to the roll-up at $Re = 250000$, 380000 and 850000 are 5.0, 10.4 and 20.4, respectively.

Figure 3.22(a) shows the frequency peaks observed from the power spectra in the shear layer and Karman vortex shedding frequency depend-

ing on the Reynolds number. At $Re = 60000$, two peaks are observed. A higher one corresponds to the shear layer roll-up and the other one corresponds to the vortex pairing process. On the other hand, for the critical and the super-critical regime, sub-harmonic peak is not observed and the frequency for the peak increases as the Reynolds number increases. The frequency for the Karman vortex shedding also increases as the Reynolds number increases. Figure 3.22(b) shows the frequency ratio between the shear layer frequency and the Karman vortex frequency. A scaling law for the subcritical Reynolds numbers was proposed by Prasad & Williamson (1997). The present result from the subcritical regime agrees well with the scaling law along with previous studies (Prasad & Williamson 1997; Norberg 1987; Wei & Smith 1986; Bloor 1964; Okamoto *et al.* 1981). Note that the present result from the sub-harmonic frequency peak also agrees well with the previous studies (Mihailovic & Corke 1997; Ahmed & Wagner 2003). However, for the critical and the super-critical regimes, the deviation from the scaling law is observed indicating that the scaling law from the sub-critical regime might not be valid in the critical and the super-critical regimes.

If we non-dimensionalize the shear layer frequencies with the mean momentum thickness and the external azimuthal velocity at the separation point, the frequencies of the shear layer vortices for the critical and the super-critical regimes collapse well onto a constant value which is about 0.008 (figure 3.23). This non-dimensional frequency is denoted as St_θ and the St_θ in the subcritical regime is much higher than St'_θ s observed in the critical and super-critical regimes. The St'_θ s for the critical and super-critical regimes in the present study are much less than those for the backward facing step (Kim *et al.* 2007) and a circular jet flow

(Zaman & Hussain 1980) and are slightly larger than that for the flat plate boundary layer with adverse pressure gradient (Pauley *et al.* 1990). It indicates that although the roll-up of the shear layer occurs for the whole regimes, the transition in the shear layer changes from free mixing layer type to boundary layer with the adverse pressure gradient type during the drag crisis. Also, effect of the cylinder surface on the shear layer roll-up is non-negligible for the critical regime.

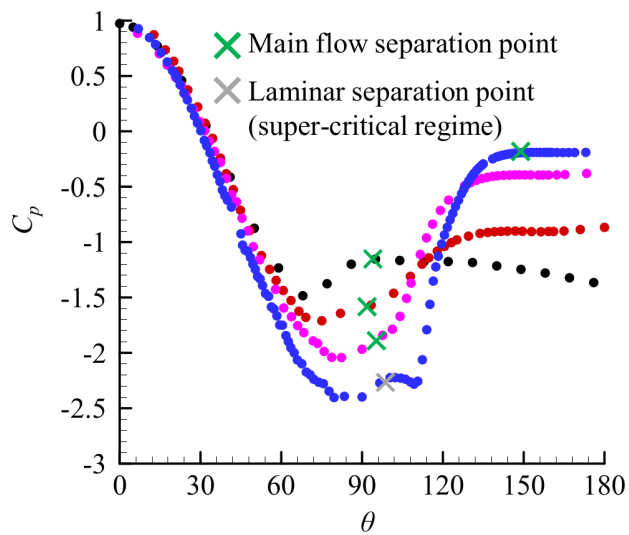


FIGURE 3.1. Surface pressure coefficients along the azimuthal direction. The separation point is shown with X symbols. \bullet , $Re = 60000$; \bullet , $Re = 250000$; \bullet , $Re = 380000$; \bullet , $Re = 850000$.

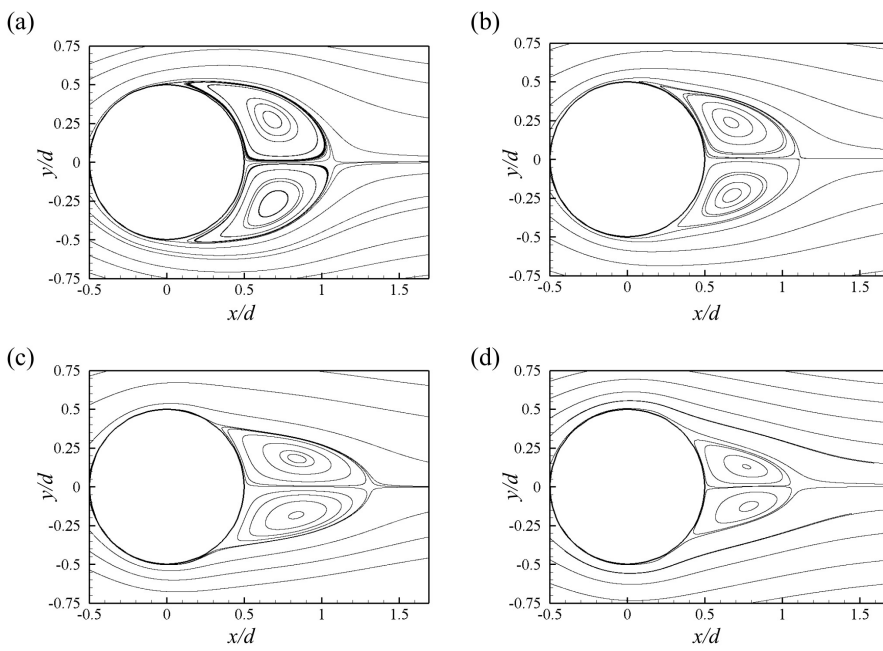


FIGURE 3.2. Mean streamlines: (a) $Re = 60000$; (b) 250000 ; (c) 380000 ; (d) 850000 .

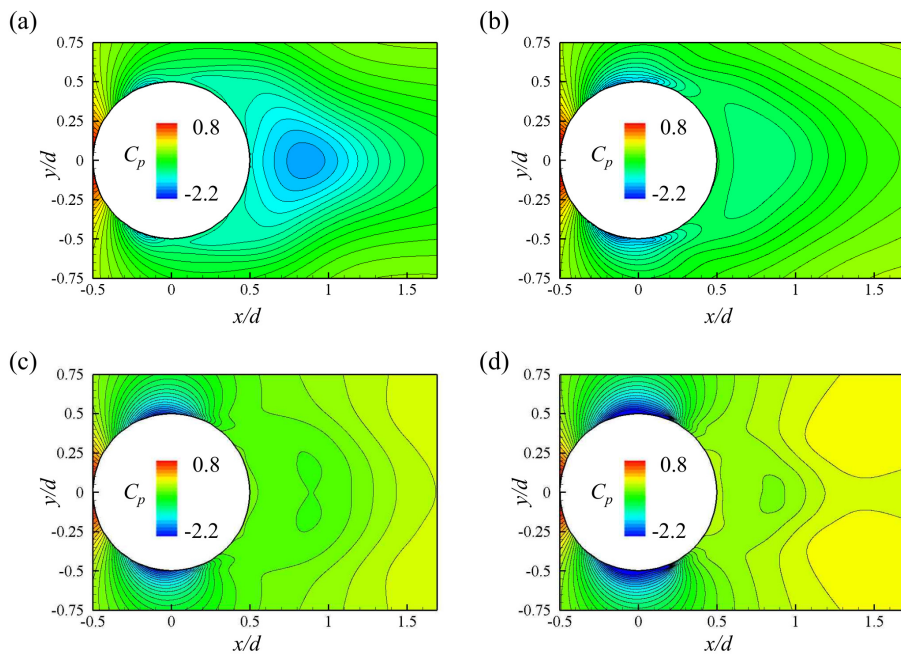


FIGURE 3.3. Mean pressure coefficients: (a) $Re = 60000$; (b) 250000; (c) 380000; (d) 850000.

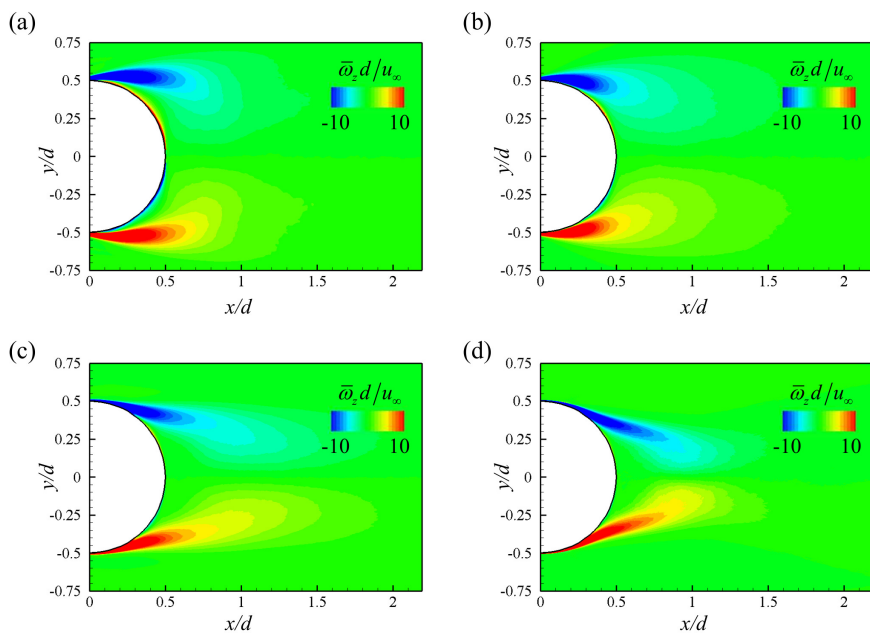


FIGURE 3.4. Mean spanwise vorticity: (a) $Re = 60000$; (b) 250000; (c) 380000; (d) 850000.

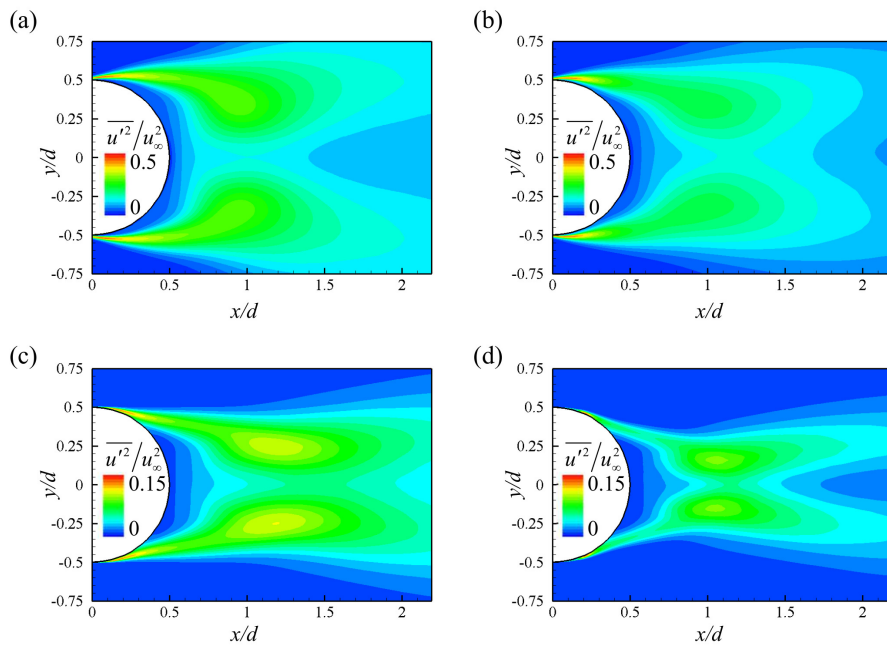


FIGURE 3.5. Reynolds normal stresses in streamwise direction: (a) $Re = 60000$; (b) 250000; (c) 380000; (d) 850000.

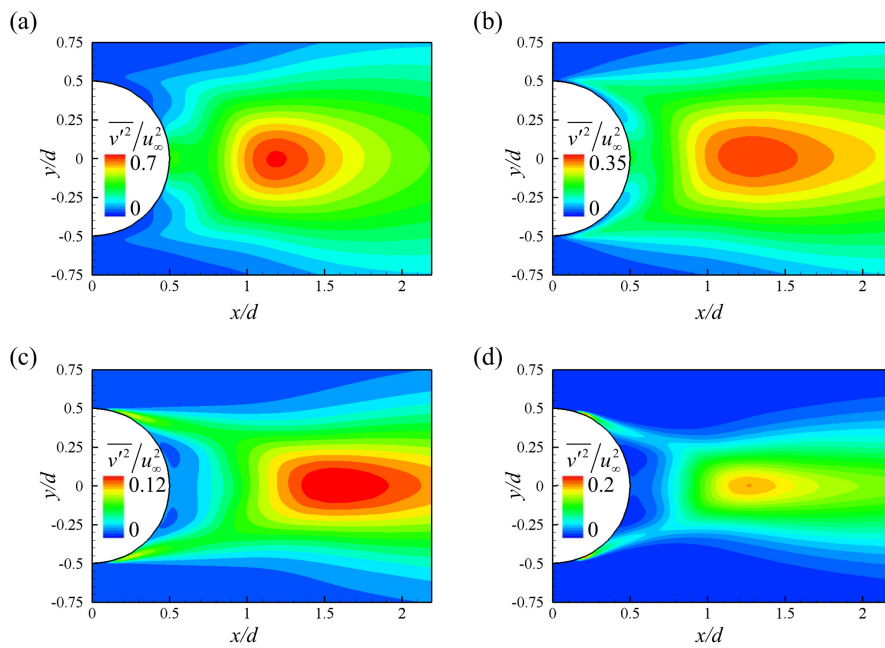


FIGURE 3.6. Reynolds normal stresses in transverse direction: (a) $Re = 60000$; (b) 250000; (c) 380000; (d) 850000.

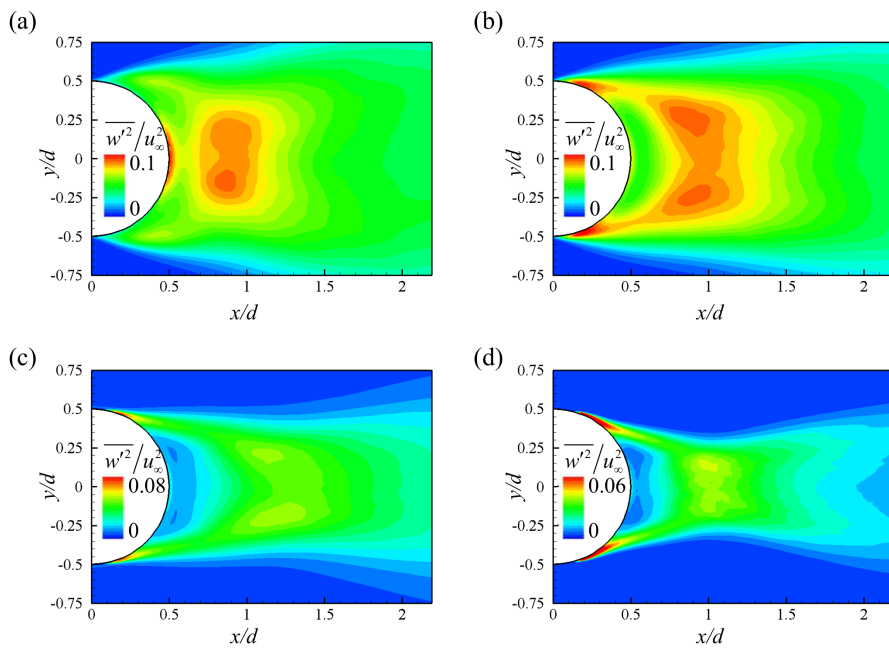


FIGURE 3.7. Reynolds normal stresses in spanwise direction: (a) $Re = 60000$; (b) 250000; (c) 380000; (d) 850000.

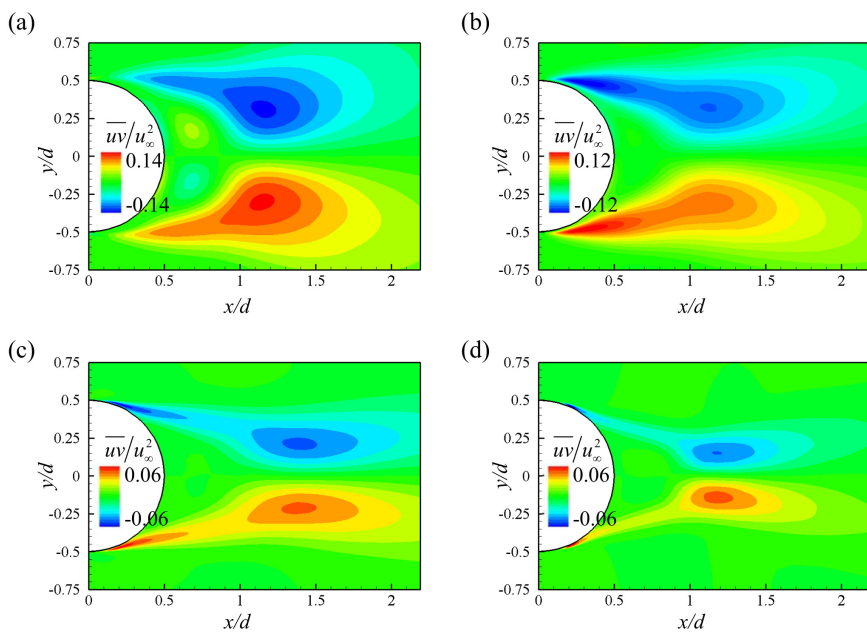


FIGURE 3.8. Reynolds shear stresses: (a) $Re = 60000$; (b) 250000; (c) 380000; (d) 850000.

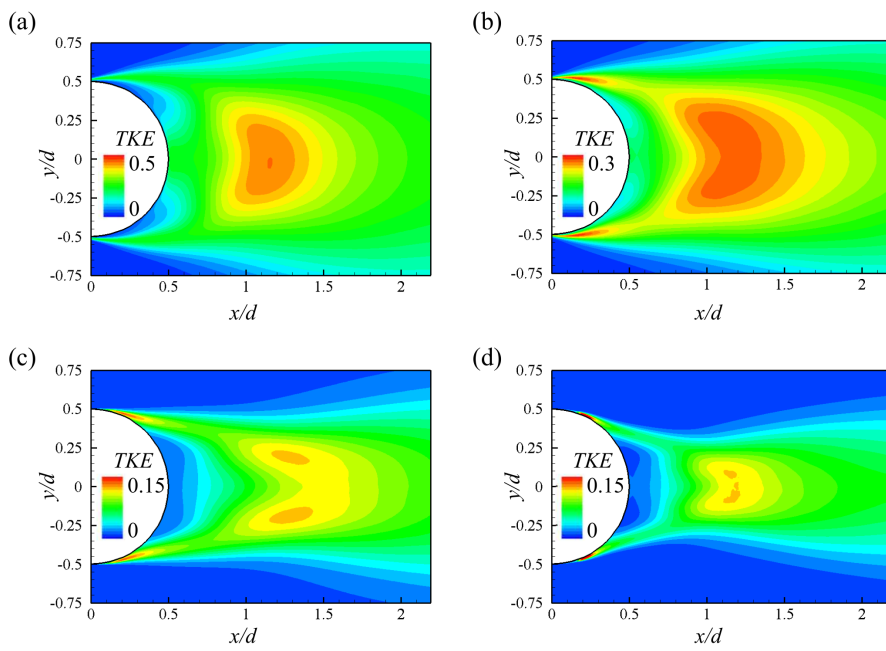


FIGURE 3.9. Turbulent kinetic energy: (a) $Re = 60000$; (b) 250000; (c) 380000; (d) 850000.

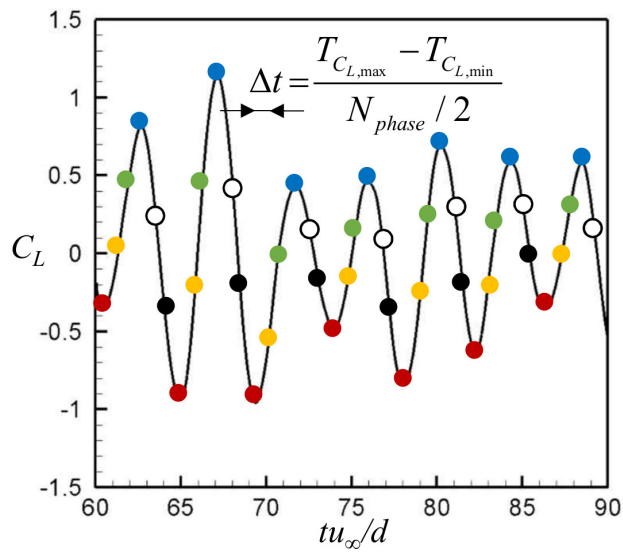


FIGURE 3.10. Definition for each phase from the time signal of the lift coefficients at $Re = 250000$.

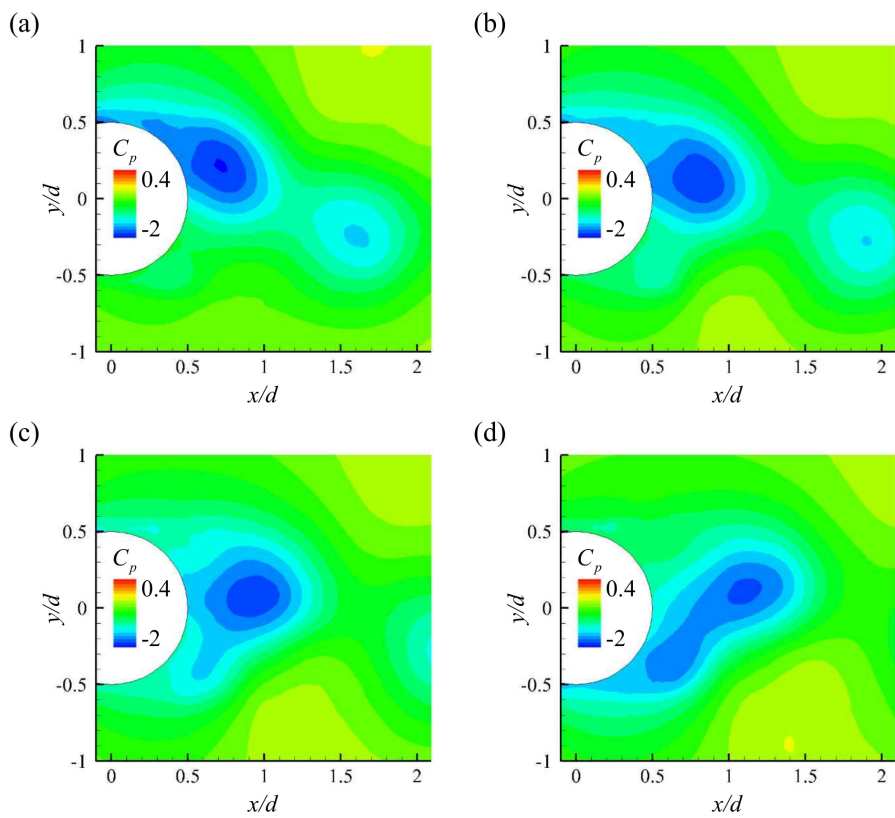


FIGURE 3.11. Phase-averaged pressure coefficients at $Re = 60000$: (a) 0 ($C_{L,max}$); (b) $\pi/5$; (c) $2\pi/5$; (d) $3\pi/5$.

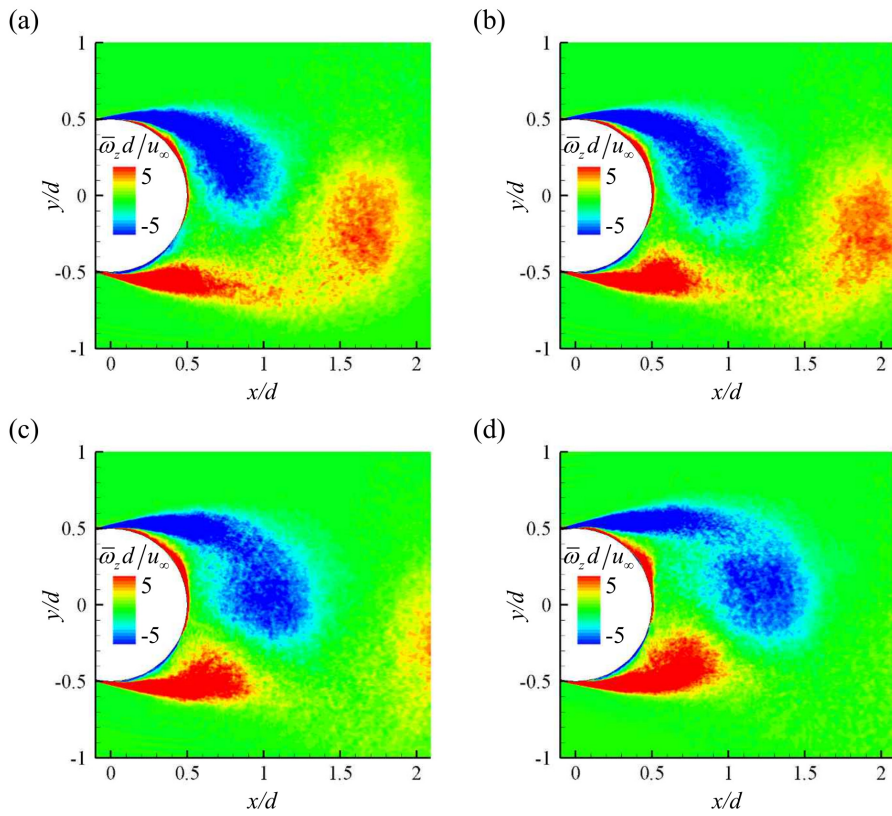


FIGURE 3.12. Phase-averaged spanwise vorticity contours at $Re = 60000$: (a) 0 ($C_{L,max}$); (b) $\pi/5$; (c) $2\pi/5$; (d) $3\pi/5$.

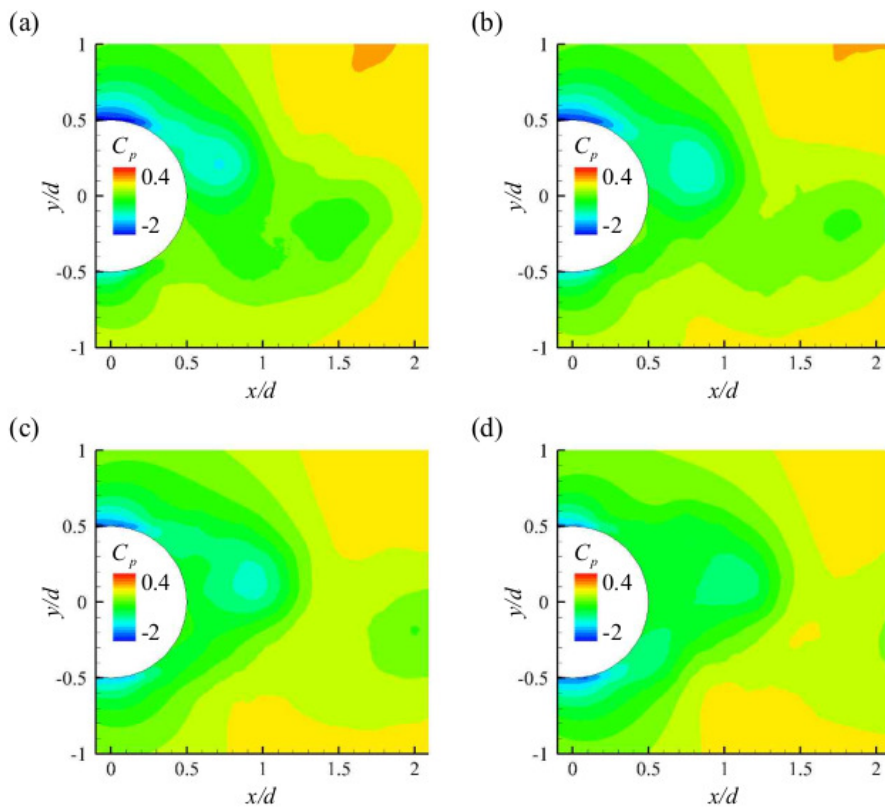


FIGURE 3.13. Phase-averaged pressure coefficients at $Re = 250000$: (a) 0 ($C_{L,max}$); (b) $\pi/5$; (c) $2\pi/5$; (d) $3\pi/5$.

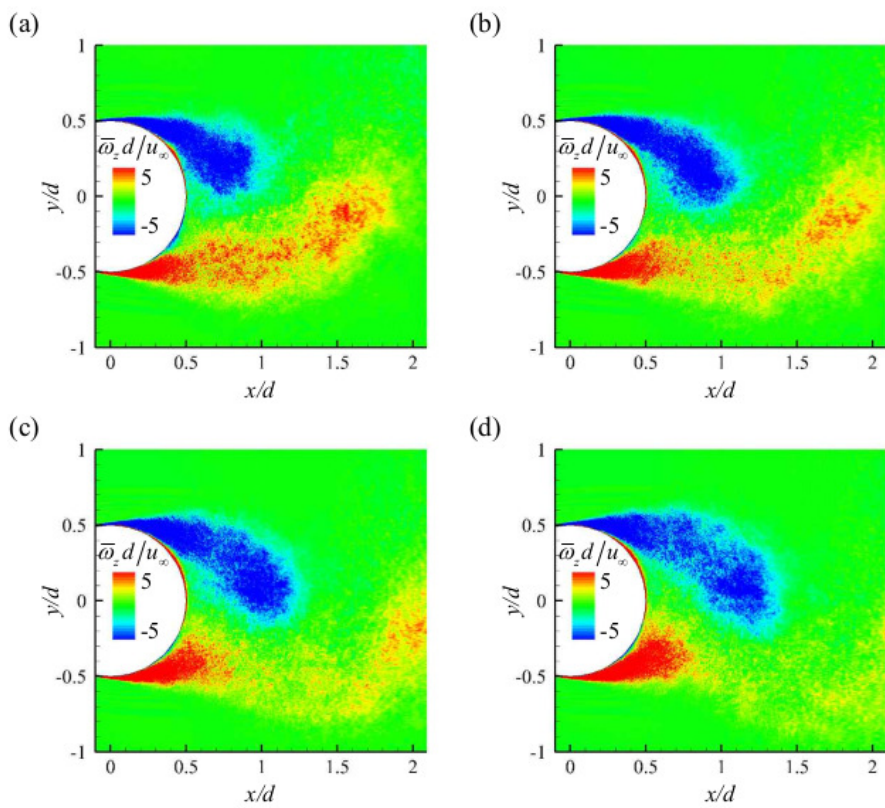


FIGURE 3.14. Phase-averaged spanwise vorticity contours at $Re = 250000$: (a) $0 (C_{L,max})$; (b) $\pi/5$; (c) $2\pi/5$; (d) $3\pi/5$.

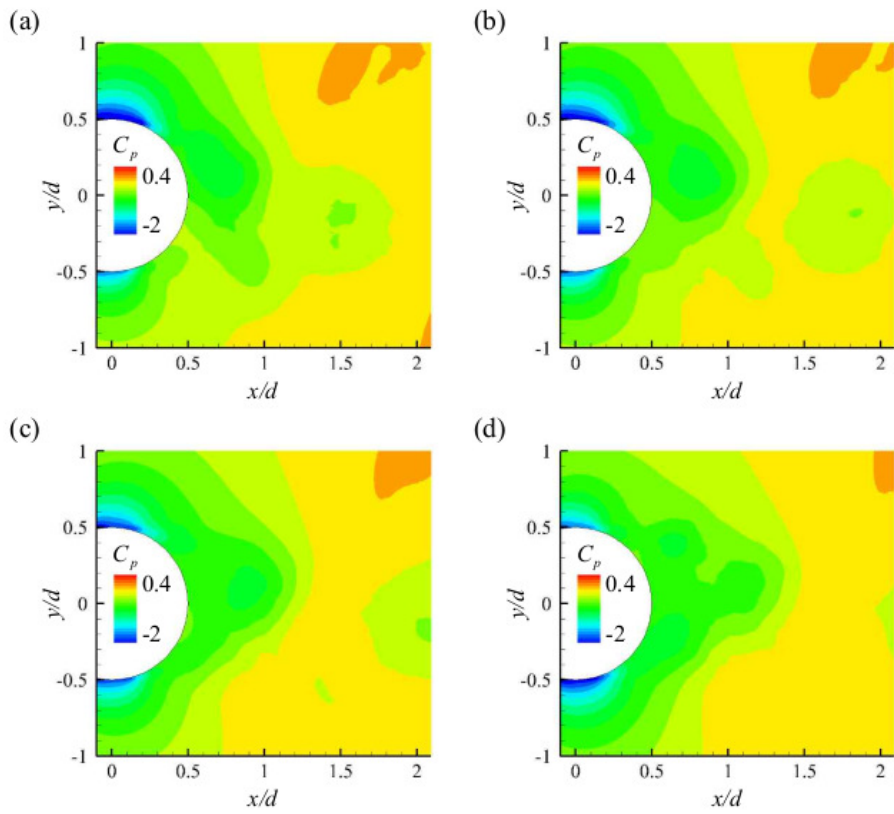


FIGURE 3.15. Phase-averaged pressure coefficients at $Re = 380000$: (a) 0 ($C_{L,max}$); (b) $\pi/5$; (c) $2\pi/5$; (d) $3\pi/5$.

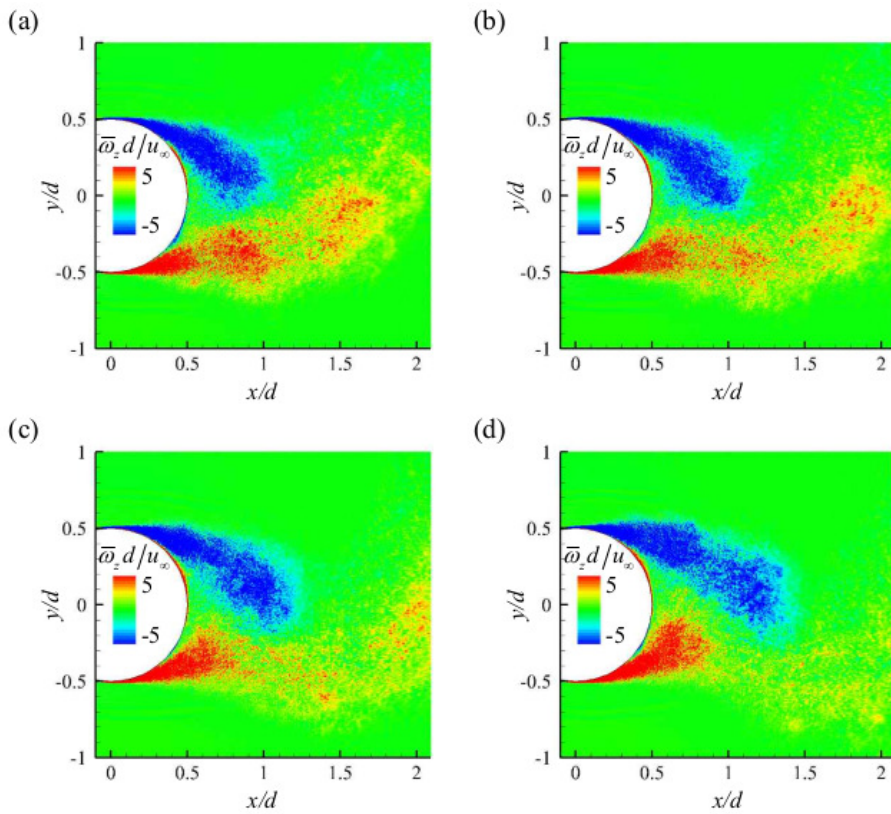


FIGURE 3.16. Phase-averaged spanwise vorticity contours at $Re = 380000$: (a) $0 (C_{L,max})$; (b) $\pi/5$; (c) $2\pi/5$; (d) $3\pi/5$.

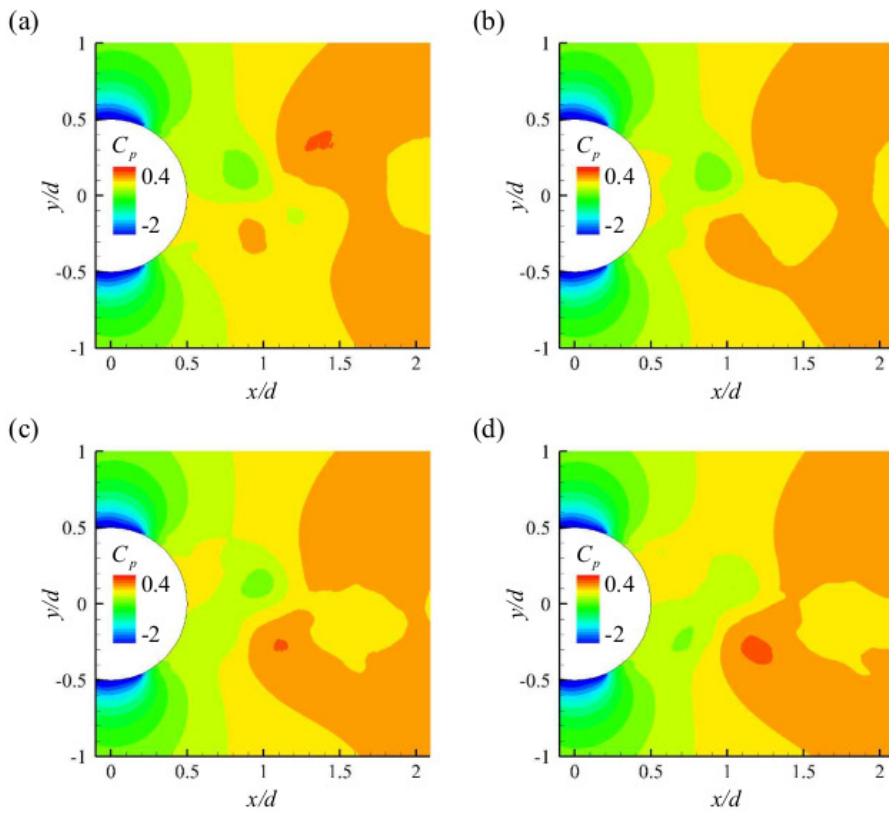


FIGURE 3.17. Phase-averaged pressure coefficients at $Re = 850000$: (a) 0 ($C_{L,max}$); (b) $\pi/5$; (c) $2\pi/5$; (d) $3\pi/5$.

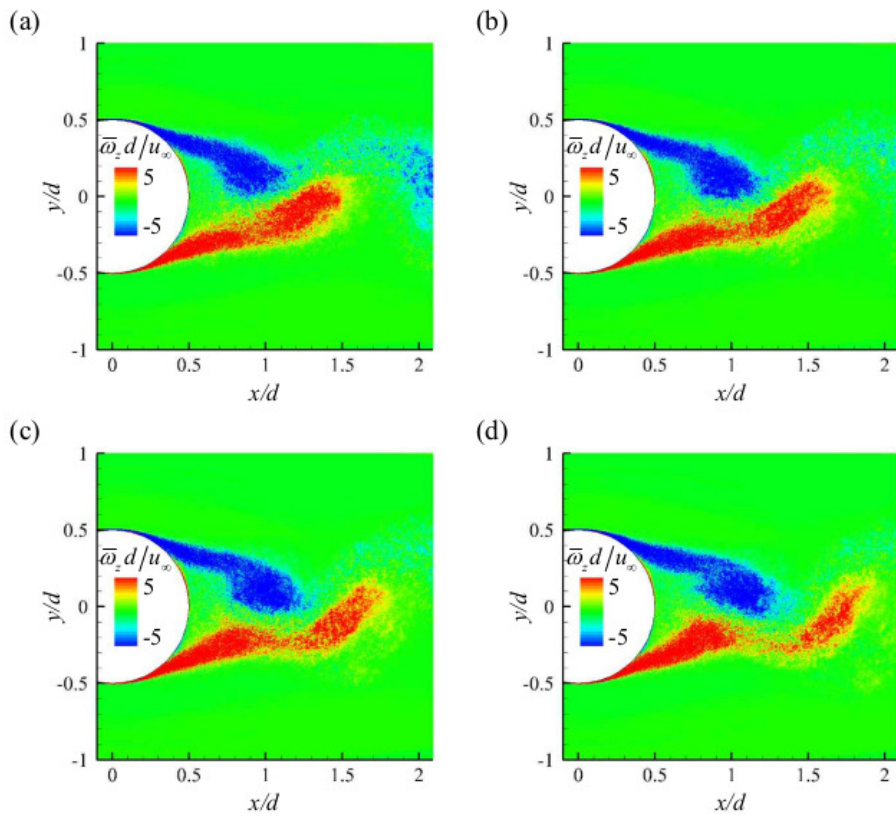


FIGURE 3.18. Phase-averaged spanwise vorticity contours at $Re = 850000$: (a) 0 ($C_{L,max}$); (b) $\pi/5$; (c) $2\pi/5$; (d) $3\pi/5$.

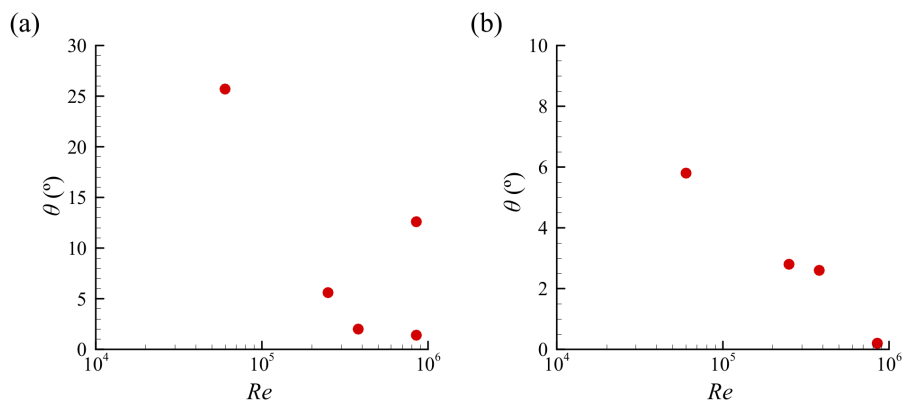


FIGURE 3.19. Angular fluctuation during Karman vortex shedding obtained from the phase-averaged flow fields: (a) separation point; (b) stagnation point.

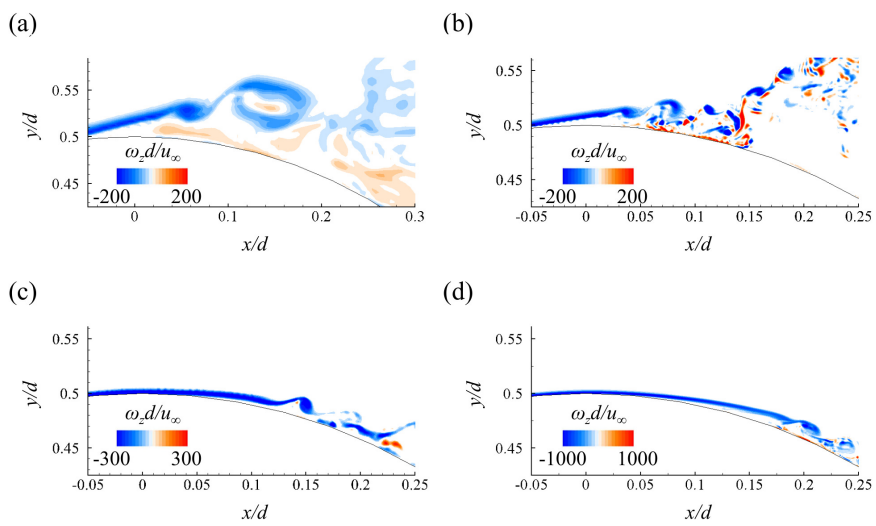


FIGURE 3.20. Instantaneous spanwise vorticity contours: (a) $Re = 60000$; (b) 250000 ; (c) 380000 ; (d) 850000 .

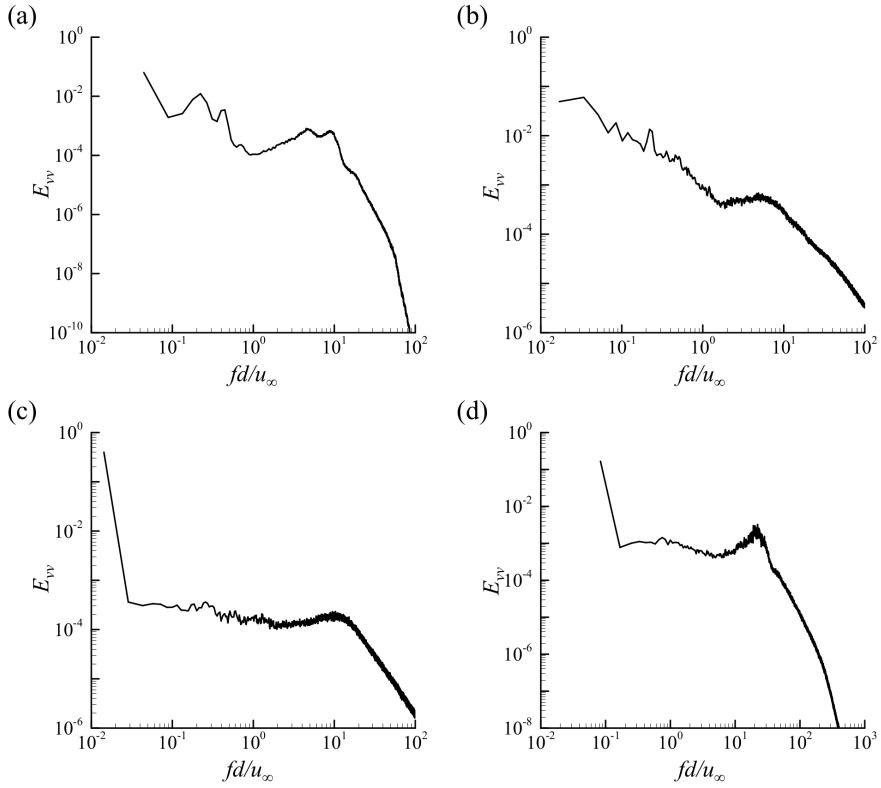


FIGURE 3.21. Power spectral density at the separated shear layer: (a) $Re = 60000$, $x/d = 0.096$, $y/d = 0.542$; (b) $Re = 250000$, $x/d = 0.096$, $y/d = 0.542$; (c) $Re = 380000$, $x/d = 0.133$, $y/d = 0.497$; (d) $Re = 850000$, $x/d = 0.174$, $y/d = 0.479$.

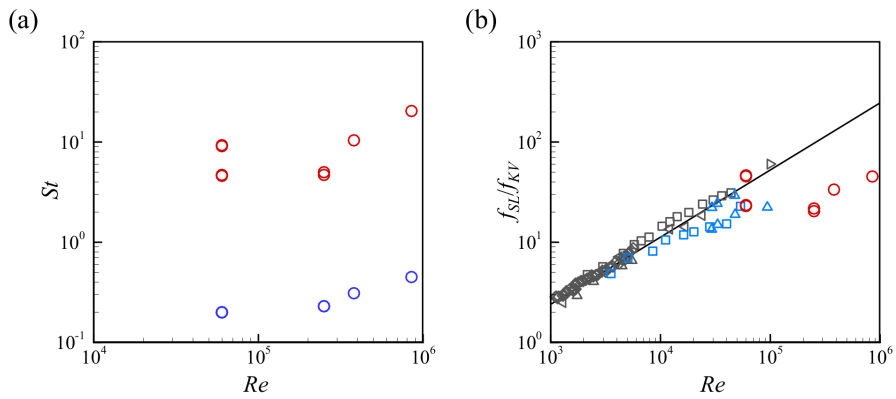


FIGURE 3.22. Frequencies of the shear layer vortices and the Karman vortices: (a) the Strouhal number (fd/u_∞); (b) frequency ratio (f_{SL}/f_{KV}). \circ , shear layer vortex; \circ , Karman vortex; \diamond Prasad & Williamson (1997); \square , Norberg (1987); \triangleright , Wei & Smith (1986); \triangleleft , Bloor (1964); \triangle , Okamoto *et al.* (1981); \square , Mihailovic & Corke (1997); \triangle , Ahmed & Wagner (2003).

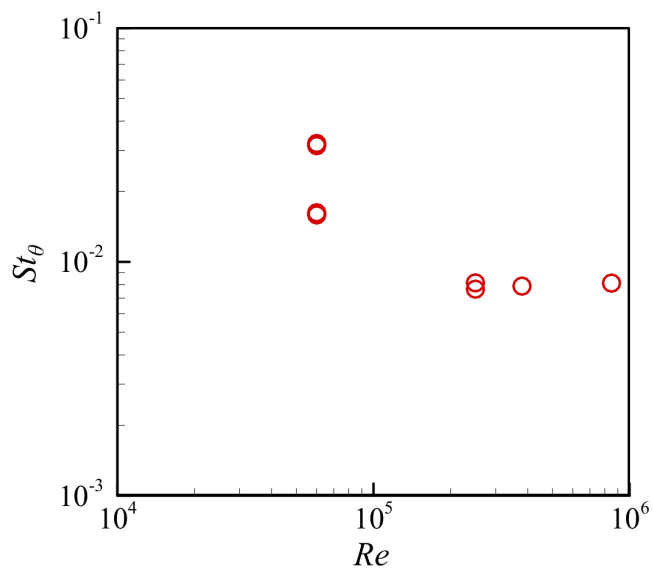


FIGURE 3.23. The shear layer frequency normalized by the momentum thickness and the external azimuthal velocity at the separation point.

Chapter 4

Conclusions

In the present study, large eddy simulations of flows around a circular cylinder in the subcritical, critical and super-critical regimes using an immersed boundary method were conducted. The Reynolds numbers considered in the study were 60000 for the subcritical regime, 250000 and 380000 for the critical regime, and 850000 for the super-critical regime. The drag coefficients and the Strouhal numbers of the present simulation agreed well with those of previous studies.

From the mean flow field, a clear difference was observed in the surface pressure distribution between the subcritical regime and the other regimes. After laminar flow separation, the wide region of the favorable surface pressure gradient was observed at the subcritical Reynolds number, whereas the wide regions of pressure recovery were observed at the critical and the super-critical Reynolds numbers. At the subcritical Reynolds number, the recirculation bubble was wide and relatively strong pressure gradient was observed inside the bubble. The maximum Reynolds normal stress in the spanwise direction was observed at the centerline

location very close to the cylinder base. At the critical and the super-critical Reynolds numbers, the separated shear layer right downstream of the mean separation point is located close to the cylinder surface and the turbulent kinetic energy and the Reynolds shear stress were relatively strong at the shear layer (compared to the wake region).

To investigate the unsteady flow related to the Karman vortex formation, a phase averaging was conducted. The minimum of the pressure field was observed in the center of the vortex at the subcritical regime while that was observed in the cylinder surface at the other regimes. The fluctuations of the laminar separation point and the stagnation point decreased as the Reynolds number increased.

From the instantaneous flow fields, vortex pairing was observed in the shear layer only at the subcritical regime. The frequency of the shear layer vortex in the critical and super-critical regimes increased as the Reynolds number increased but the frequency normalized with external azimuthal velocity and the momentum thickness at the laminar separation point was almost constant regardless of the Reynolds numbers.

Part II.

Universal relations between the drag and the wake of a circular cylinder

This part is based on “**Jin, D.**, Wu, Z. & Choi, H. 2021 A predictive model of the drag coefficient of a circular cylinder. *Phys. Fluids* **33**, 111702” .

Chapter 1

Introduction

Understanding the relation between the drag force acting on a body and the characteristics of the wake is a primary concern in many external flow researches. The mean drag coefficient of a two-dimensional body can be obtained from the mean momentum deficit (momentum thickness) at the far wake (Tennekes & Lumley 1972).

$$C_D = \frac{2}{d} \int_{-\infty}^{\infty} \left(\frac{\bar{u}}{u_{\infty}} - \frac{\bar{u}^2}{u_{\infty}^2} \right) dy. \quad (1.1)$$

This method is attractive in a way that one can measure the drag without the use of experimental apparatus on a body surface. However, at the near wake where many experimental studies on the flows around two-dimensional bodies have been conducted, the relation no longer holds and the contribution of the pressure distribution at the wake to the drag is non-negligible.

Dimotakis (1977) proposed a method to calculate the drag by modeling the effect of the pressure with Reynolds normal stresses and a displacement thickness of the wake. Wen *et al.* (2004) conducted an experiment on the flow around a circular cylinder using a soap film tunnel. They claimed

that the drag coefficient obtained by the model proposed by Dimotakis (1977) showed a good agreement with two-dimensional computations of Henderson (1995) for Reynolds number 35 to 560 but their measurements were obtained far from the body only ($x/d \geq 30$). Apart from the method of Dimotakis (1977), Townsend (1956) suggested the relation between the drag and the velocity field by modeling the pressure effect with a Reynolds normal stress term. Antonia & Rajagopalan (1990) conducted an experimental study on the flow over a circular cylinder at $Re = 5600$ to validate the drag prediction model suggested by Townsend (1956) in the near wake region assuming the velocity outside of the wake as freestream velocity. They suggested that the relation for the far wake region was sufficient to predict the drag coefficient for $x/d \geq 30$ but the contribution from the Reynolds normal stresses was non-negligible for $5 \leq x/d < 30$. Based on the analysis, the model has been adopted to measure the drag coefficients for various two-dimensional bodies such as rectangular cylinders (Mohebi *et al.* 2017), flat plates with various corner shapes (Xu *et al.* 2015) and airfoils (Zhou *et al.* 2011). Also, the merit of the model that there is no need for any surface instrumentation enabled a wide usage of the model especially in the flow control studies such as circular cylinders with bleed near separation points (Shi & Feng 2015), with plasma actuation (Bhattacharya & Gregory 2015), with rough hydrophobic surfaces (Kim *et al.* 2015) and with upstream splitter plate (Zhou *et al.* 2019).

However, the model could not always guarantee the accurate prediction of the drag at the near wake. Son & Cetiner (2016) measured velocity profiles in the near wake of a circular cylinder using a 2D2C DPIV system with Reynolds numbers ranging from 100 to 1250. The measured range of the wake width was limited to $-4 \leq y/d \leq 4$ and they obtained under-

estimated drag coefficients for $x/d \geq 5$. Also, there is no clear guideline for the integration range of the models so that most studies have adopted the range as wide as possible.

The characteristic coherent structure in the two-dimensional bluff body wake is the Karman vortex. From a sufficiently high Reynolds number ($Re \sim 46$), the Karman vortex street is observed in the wake. A universal Strouhal number for the wakes of two-dimensional bluff bodies with fixed and free separation point, vibrating bluff bodies has been studied. Different from the conventional definition of the Strouhal number which is the frequency normalized by the diameter of the cylinder and the free-stream velocity, the universal Strouhal number is defined by normalizing the frequency with the characteristic length and velocity scales of the wake.

Roshko (1954) proposed a universal Strouhal number of various bluff bodies based on the velocity scale from the base pressure coefficient and the wake width from a free-streamline model whose input is the base pressure coefficient. The velocity scale from the base pressure is written as, $u_b = u_\infty \sqrt{1 - C_{pb}}$ and the physical meaning of the velocity is the approximation of the velocity at the edge of the boundary layer at the separation point. Based on this assumption, he suggested a free streamline model using a notched hodograph theory to define a width of the wake and showed that the Strouhal numbers based on these scales were nearly constant regardless of the various geometries of two-dimensional bluff bodies. However, the model can only be adopted for the subcritical wake and for each shape of the body, a corresponding model is required. Also, it is difficult to extend this concept to vibrating bodies or the bodies with confinement.

Therefore, researchers have tried to obtain a characteristic length scale of the wake from the direct measurement inside the vortex formation region (Calvert 1967; Simmons 1977; Griffin 1978; Rodríguez *et al.* 2015). A common definition for the length scale is the transverse distance between the locations of maximum RMS streamwise velocity. The streamwise location for defining the characteristic wake width for the universal Strouhal number is the location which is used for defining vortex formation length (l_f). Simmons (1977); Calvert (1967) defined the formation location as the streamwise location where the minimum pressure coefficient is observed on wake centerline. Simmons (1977) conducted experimental studies on various two-dimensional bluff bodies and axisymmetric bodies and obtained almost constant Strouhal numbers for the 2d bodies and the axisymmetric bodies, respectively. Griffin (1978); Rodríguez *et al.* (2015) defined the vortex formation location as the location where the wake width becomes minimum. Griffin (1978) and Rodríguez *et al.* (2015) conducted experiments on vibrating cylinders at subcritical Reynolds numbers and on the stationary circular cylinder at critical and super-critical Reynolds numbers, respectively, and they obtained universal Strouhal numbers, 0.178 and 0.164, respectively.

Also, a wake drag coefficient which is defined as the mean drag normalized by the characteristic length and velocity scales of the wake also showed a similarity (Griffin 1980). Based on the non-dimensional parameters which are independent of the Reynolds numbers, Griffin (1980) suggested a non-dimensional parameter which relates the drag and the vortex shedding frequency, $C_D St / (1 - C_{pb})^{1.5}$ which is nearly constant regardless of the Reynolds number.

The objective of present study is to develop an improved drag predic-

tion model based on the velocity profiles at the near wake and to suggest universal scaling laws with a consistent definition of the length and velocity scales at the vortex formation region. Numerical simulations of flows over a circular cylinder at various Reynolds numbers are conducted in the study and the numerical methods are described in chapter 2. In chapter 3, we apply a momentum integral theory to derive a new model and investigate the validity of the assumptions on the simulation results. The drag coefficients predicted from the present model is compared with those of the numerical simulations and aforementioned models. In chapter 4, we propose a new scales for length and velocity inside the wakes and calculate a universal Strouhal number. Also, based on the control volume analysis, we conduct a budget analysis for the drag inside the vortex formation region and suggest a new scaling law regarding the drag coefficient.

Chapter 2

Numerical methods

2.1. Simulation cases

In this part, we need to simulate a wide range of Reynolds numbers to study universal characteristics of the flow over a circular cylinder. The Reynolds numbers considered in the present study are 50 for laminar flow, 220 for transition in the wake, 3900 for transition in the shear layer, 60000 for the upper subcritical regime, 250000 and 380000 for critical regime and 850000 for super-critical regime, respectively. For laminar and low-Reynolds-number turbulent flows, direct numerical simulation (without turbulence model) is performed, whereas large eddy simulation (LES) is conducted for higher Reynolds numbers (see table 2.1). Numerical schemes and boundary conditions are the same with those from Part 1. Corresponding computational domain sizes and numbers of grid points are also listed in table 2.1.

2.2. Validation

To check the validity of our simulation results, the mean drag coefficients and the Strouhal numbers are compared with the previous studies (Wieselsberger 1922; Roshko 1954; Achenbach & Heinecke 1981; Schewe 1983; Williamson 1992; Kim & Choi 2005; Cadot *et al.* 2015) in figure 2.1. The mean drag coefficient is defined as $C_D = 2\bar{D}/\rho u_\infty^2 dL_z$, where D and ρ denote the drag and the density of the fluid, respectively. The Strouhal number is defined as $St = fd/u_\infty$, where f represents the frequency of the Karman vortex shedding. The drag coefficients and the Strouhal numbers from the present simulation agree well with previous studies.

| Re | DNS/LES | L_x/d | L_y/d | L_z/d | N_x | N_y | N_z |
|--------|---------|---------|---------|----------|-------|-------|-------|
| 50 | DNS | 200 | 200 | π | 513 | 241 | - |
| 220 | DNS | 90 | 100 | π | 385 | 217 | 80 |
| 3900 | DNS | 30 | 50 | π | 1025 | 513 | 128 |
| 60000 | LES | 30 | 50 | π | 1025 | 641 | 80 |
| 250000 | LES | 24 | 50 | 0.5π | 1793 | 1025 | 128 |
| 380000 | LES | 24 | 50 | 0.5π | 2048 | 1169 | 128 |
| 850000 | LES | 20 | 30 | 0.5 | 3585 | 2369 | 64 |

TABLE 2.1. Summary of the simulations.

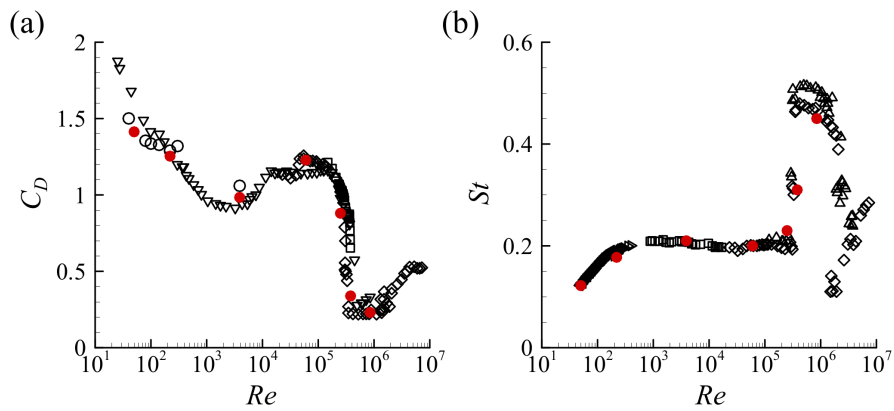


FIGURE 2.1. Variations of the drag coefficient and Strouhal number with the Reynolds number: (a) C_D vs. Re ; (b) St vs. Re . Present (red circle), Wieselsberger (1922) (∇), Roshko (1954) (\triangleleft), Achenbach & Heinecke (1981) (\triangle), Schewe (1983) (\diamond), Williamson (1992) (\triangleright), Kim & Choi (2005) (\circ), Cadot *et al.* (2015) (\square).

Chapter 3

A predictive model of the drag coefficient based on the velocity information in the wake

3.1. Formulation for the drag coefficient model

Let us consider a control volume composed of the inlet, outlet and two streamlines enclosing a two-dimensional bluff body, as shown in figure 3.1, where s and n , l_s , and h and H denote the coordinates along the streamline and normal to the streamline, the length of the streamline from the inlet to the outlet, and the widths of the inlet and outlet, respectively. At the outlet, the maximum velocity u_o locates at $y = y_o$, where $y = 0$ is the centerline. The mass conservation for this control volume provides

$$\int_{-\frac{h}{2}}^{\frac{h}{2}} \rho u_{\infty} dy = \int_{-\frac{H}{2}}^{\frac{H}{2}} \rho \bar{u} dy, \quad (3.1)$$

where ρ is the density, u_{∞} is the free-stream velocity, and the overbar denotes time averaging. From the momentum conservation in the stream-

wise direction, we have

$$\frac{\partial}{\partial t} \int \rho u dV + \oint \rho u (\mathbf{u} \cdot \hat{\mathbf{n}}) dA = - \oint p (\hat{\mathbf{x}} \cdot \hat{\mathbf{n}}) dA + \oint \mu \frac{\partial u}{\partial n} dA - D, \quad (3.2)$$

where \mathbf{u} is the instantaneous velocity vector, $\hat{\mathbf{n}}$ is the out-normal vector from the control surface, p is the instantaneous pressure, μ is the viscosity, and D is the instantaneous drag on the bluff body, respectively. With time averaging, (3.2) becomes

$$\frac{\bar{D}}{L_z} = - \oint \overline{\rho u (\mathbf{u} \cdot \hat{\mathbf{n}})} dl - \oint \bar{p} (\hat{\mathbf{x}} \cdot \hat{\mathbf{n}}) dl + \oint \mu \frac{\partial \bar{u}}{\partial n} dl, \quad (3.3)$$

where L_z is the spanwise length. The three terms on the right hand side of (3.3) become

$$- \oint \overline{\rho u (\mathbf{u} \cdot \hat{\mathbf{n}})} dl = \int_{-\frac{H}{2}}^{\frac{H}{2}} \rho \bar{u} u_\infty dy - \int_{-\frac{H}{2}}^{\frac{H}{2}} \rho (\bar{u}^2 + \overline{u'^2}) dy, \quad (3.4)$$

$$- \oint \bar{p} (\hat{\mathbf{x}} \cdot \hat{\mathbf{n}}) dl = \int_{-\frac{h}{2}}^{\frac{h}{2}} p_\infty dy - \int_{-\frac{H}{2}}^{\frac{H}{2}} \bar{p} dy - 2 \int_0^{l_s} \bar{p} (\hat{\mathbf{x}} \cdot \hat{\mathbf{n}}) ds, \quad (3.5)$$

$$+ \oint \mu \frac{\partial \bar{u}}{\partial n} dl = - \int_{-\frac{h}{2}}^{\frac{h}{2}} \mu \frac{\partial \bar{u}}{\partial x} dy + \int_{-\frac{H}{2}}^{\frac{H}{2}} \mu \frac{\partial \bar{u}}{\partial x} dy + 2 \int_0^{l_s} \mu \frac{\partial \bar{u}}{\partial n} ds, \quad (3.6)$$

where the prime denotes the fluctuations.

We assume $\bar{p} \approx p_\infty$, $\hat{\mathbf{x}} \cdot \hat{\mathbf{n}} \approx 0$ and $\partial \bar{u} / \partial n \approx 0$ on the streamlines (figure 3.1), when they locate far away from the bluff body. Also, we assume $\partial \bar{u} / \partial x \approx 0$ at the inlet and outlet, when the inlet and outlet locate away from the bluff body (the validity of these assumptions are examined later in this paper). Then, (3.3) with (3.4 - 3.6) reads

$$\frac{\bar{D}}{L_z} = \int_{-\frac{H}{2}}^{\frac{H}{2}} \rho (\bar{u} u_\infty - \bar{u}^2 - \overline{u'^2}) dy + \int_{-\frac{H}{2}}^{\frac{H}{2}} (p_\infty - \bar{p}) dy. \quad (3.7)$$

The drag coefficient is obtained as

$$C_D = \frac{2}{d} \int_{-\frac{H}{2}}^{\frac{H}{2}} \left(\frac{\bar{u}}{u_\infty} - \frac{\bar{u}^2}{u_\infty^2} - \frac{\overline{u'^2}}{u_\infty^2} \right) dy - \frac{1}{d} \int_{-\frac{H}{2}}^{\frac{H}{2}} C_p dy, \quad (3.8)$$

where $C_D = \bar{D}/(\frac{1}{2}\rho u_\infty^2 L_z d)$ and $C_p = (\bar{p} - p_\infty)/(\frac{1}{2}\rho u_\infty^2)$.

Now, let us model the pressure term in (3.8). We first divide the outlet $(-H/2, H/2)$ into two regions, i.e., inviscid and wake regions, respectively. The boundary between two regions is set to be the location of maximum mean streamwise velocity u_o at the outlet, i.e., $\bar{u} = u_o$ at $y = y_o$ (see figure 3.1). In an inviscid region ($y > y_o$), the Bernoulli equation is valid, $\bar{v}^2 \ll \bar{u}^2$, and the velocity fluctuations are negligible. Thus, the pressure coefficient becomes

$$C_{p,inv} = 1 - \frac{\bar{u}^2 + \bar{v}^2 + \overline{u'^2} + \overline{v'^2} + \overline{w'^2}}{u_\infty^2} \approx 1 - \frac{\bar{u}^2}{u_\infty^2}. \quad (3.9)$$

In a wake region ($y \leq y_o$) away from the bluff body, the relation between the pressure and the velocity field can be obtained using the transverse momentum equation using turbulent boundary-layer approximation (Tennekes & Lumley 1972; Antonia & Rajagopalan 1990). By adopting the turbulent boundary-layer approximation, the transverse momentum equation can be written as,

$$\frac{1}{\rho} \frac{\partial \bar{p}}{\partial y} + \frac{\partial \overline{v'^2}}{\partial y} = 0. \quad (3.10)$$

Integrating (3.10) from y to y_o provides

$$\bar{p}_0 = \bar{p} + \rho \overline{v'^2}. \quad (3.11)$$

Then, the mean pressure in the wake becomes

$$\bar{p} - p_\infty = -\rho \overline{v'^2} + (\bar{p}_0 - p_\infty). \quad (3.12)$$

By applying the Bernoulli equation to the second term on the right hand side of (3.12), we get

$$C_{p,wake} = -\frac{2\overline{v'^2}}{u_\infty^2} + 1 - \frac{u_0^2}{u_\infty^2}. \quad (3.13)$$

With (3.9) and (3.13), (3.8) becomes

$$C_D = \frac{2}{d} \int_{-\frac{H}{2}}^{\frac{H}{2}} \left(\frac{\bar{u}}{u_\infty} - \frac{\bar{u}^2}{u_\infty^2} - \frac{\overline{u'^2}}{u_\infty^2} + \frac{\overline{v'^2}}{u_\infty^2} \right) dy + \frac{1}{d} \int_{-\frac{H}{2}}^{\frac{H}{2}} \left(\frac{u_w^2}{u_\infty^2} - 1 \right) dy, \quad (3.14)$$

where

$$u_w = \begin{cases} u_o & \text{for } |y| \leq y_o \\ \bar{u} & \text{for } |y| > y_o. \end{cases} \quad (3.15)$$

(3.14) is the present model for the drag coefficient on a bluff body. How much this model is accurate in estimating the drag on a bluff body depends on the streamwise location x and the size of the integral height H .

Dimotakis (1977) provided a formula for the drag coefficient as follows:

$$C_D = \frac{2}{d} \int_{-\frac{H}{2}}^{\frac{H}{2}} \left(\frac{\bar{u}}{u_\infty} - \frac{\bar{u}^2}{u_\infty^2} - \frac{\overline{u'^2}}{u_\infty^2} + \frac{\overline{v'^2}}{u_\infty^2} + \frac{\overline{v'^2}}{u_\infty^2} \right) dy + \frac{1}{d} \int_{-\frac{H}{2}}^{\frac{H}{2}} \left(\frac{\bar{u}^2|_{y=H/2}}{u_\infty^2} - 1 \right) dy. \quad (3.16)$$

Note that (3.14) and (3.16) are very similar to each other except the velocity in the second term on the right hand side. As we show later, this different choice of the velocity provides a significant difference in estimating the drag coefficient. On the other hand, Antonia & Rajagopalan (1990) suggested the following formula for the drag estimation:

$$C_D = \frac{2}{d} \int_{-\frac{H}{2}}^{\frac{H}{2}} \left(\frac{\bar{u}}{u_\infty} - \frac{\bar{u}^2}{u_\infty^2} - \frac{\overline{u'^2}}{u_\infty^2} + \frac{\overline{v'^2}}{u_\infty^2} \right) dy. \quad (3.17)$$

This formula neglected the contribution from the second term in the right hand side of (3.14).

The differences between the present model and the other models come from the different assumptions adopted to model the pressure term in Eq.

(3.8). Since Antonia & Rajagopalan (1990) assumed that the velocity outside of the wake region is equal to the free-stream velocity, the boundary between inviscid region and wake region from their analysis locates at $y = y_1$, where \bar{u} becomes u_∞ . Also, \bar{u} for $|y| > y_1$ can be approximated as u_∞ with their assumption. Then, u_w in Eq. (3.14) can be replaced by u_∞ so that Eq. (3.14) can be reduced to Eq. (3.17). Although Antonia & Rajagopalan (1990) suggested that the integral height should be as large as possible ($H \rightarrow \infty$) to contain the outside of the wake region, the applicable integral height of their model might be $H \approx 2y_1$ since they did not consider the non-uniform velocity profile for $|y| > y_1$. Note that the predicted drag coefficients from Eqs. (3.17) and (3.14) should be exactly the same only at $H = 2y_1$. On the other hand, Dimotakis (1977) claimed that the streamwise velocity outside of the wake region should be larger than the free-stream velocity due to the finite size of the domain. However, he also assumed the uniform velocity profile outside of the wake region. Therefore, his assumptions imply $u_w = u|_{y=H/2}$ with sufficiently large H which is enough to contain the outside of the wake region. Then, Eq. (3.14) becomes almost equal to Eq. (3.16). Note that \bar{v}^2/u_∞^2 in Eq. (3.16) comes from substituting $\overline{v'^2}$ with \bar{v}^2 in Eq. (3.10) and the effect from this difference is negligible ($\overline{v'^2} \gg \bar{v}^2$). Although Dimotakis (1977) anticipated that the one of the main sources of error might be the non-uniformity of the flow outside of the wake region, he did not propose the appropriate size of H to minimize the error. As we show later, we believe that $H \approx 2y_o$ should be used to adopt Eq. (3.16). Note also that the predicted drag coefficients from Eqs. (3.16) and (3.14) should be almost the same at $H = 2y_o$.

3.2. Validity of the assumptions

To check the validity of the assumptions that we used to derive the (3.14) we first conduct a control volume analysis without any assumptions. Then (3.3) with (3.4 - 3.6) reads,

$$\begin{aligned}
 C_D = & \frac{2}{d} \int_{-\frac{H}{2}}^{\frac{H}{2}} \left(\frac{\bar{u}}{u_\infty} - \frac{\bar{u}^2}{u_\infty^2} - \frac{\overline{u'^2}}{u_\infty^2} \right) dy - \frac{1}{d} \int_{-\frac{H}{2}}^{\frac{H}{2}} C_p dy + \frac{2}{u_\infty Re} \int_{-\frac{H}{2}}^{\frac{H}{2}} \frac{\partial \bar{u}}{\partial x} dy \\
 & + 2 \int_0^{l_s} \left(-\frac{C_p(\hat{\mathbf{x}} \cdot \hat{\mathbf{n}})}{d} + \frac{2}{u_\infty Re} \frac{\partial \bar{u}}{\partial n} \right) ds. \tag{3.18}
 \end{aligned}$$

The first three terms from the right-hand side of (3.18) are the integrals from the outlet while the last term is the integral from the streamlines. The first term represents the contribution from the convective flux and the second term represents that from the pressure and the third term represents that from the viscous diffusion. The last term represents the contribution from the pressure and the viscous diffusion at the streamline.

Figure 3.2(a-c) show the contributions to C_D from each term with streamwise location at $Re = 50, 3900$ and 250000 , respectively. The integration height (H) is equal to the width of the numerical domain (L_y). One can observe a similar trend regardless of the Reynolds numbers. The contributions from the convective flux are negative while those of the pressure are positive. The contributions from the viscous diffusion are negligible and those at the streamline are analytically zero by the boundary condition on the side wall. The streamline is strictly aligned to the streamwise direction so that $\hat{\mathbf{x}} \cdot \hat{\mathbf{n}}$ and the normal gradient of streamwise velocity are zero.

Many researchers have often divided the wake region close to the body into the vortex formation region (or very near wake) and near wake (Beaudan & Moin 1994; Kravchenko & Moin 2000). Beaudan & Moin (1994)

referred that the vortex formation region consists of the cylinder surface, the recirculation zone and the recovery region. The recovery region at $Re = 3900$ was defined as the region between the mean recirculation bubble closure point and $x/d = 4$ where the strong velocity and pressure gradients in streamwise direction were observed. Since the longest recirculation region is observed at $Re = 3900$ among the present simulations, $x/d > 4$ belongs to the near wake region for the present study. As most researches adopting a previous model (Antonia & Rajagopalan 1990) calculated drag coefficients at $x/d > 4$ (Feng & Wang 2014; Shi & Feng 2015; Hamed *et al.* 2017), the present analysis is mainly focused on the near wake region.

Figure 3.2(d-f) show the contributions to C_D from each term with the integration range at $x/d = 5$. The integration ranges for the maximum contribution from the convective flux are observed near $H/d \approx 4$ where they show positive values indicating that the negative contribution in figure 3.2(a-c) is the result of the wide range. The contributions from the outlet pressure distribution increase with the integration range monotonically. The contributions from the viscous diffusion at the outlet are negligible regardless of the integration range. The contributions at the streamline decrease to zero near $H/d \approx 5$. The contributions from each term at $x/d = 10$ show similar trends with those at $x/d = 5$ (figure 3.2d-i). Therefore, we can neglect the effect of viscous diffusion since the present control volume analysis mainly focused on the flow where $Re \gg 1$. One can also assume that the contribution at the streamline is negligible only with sufficient measurement range ($H/d > 5$). By neglecting the small terms, we can rewrite the equation for the drag coefficient as (3.8).

In the wake region a boundary layer approximation is applied as in

(3.10). Assuming that (3.10) is valid, \bar{p}_o should be constant along transverse direction inside the wake. To check the validity of the assumption, we compare C_p and $C_p + 2\overline{v'^2}/u_\infty^2$ in figure 3.4(a-c). The profiles of $C_p + 2\overline{v'^2}/u_\infty^2$ should be flat but they show peaks at $y/d = 0$. However, they become flat as x/d increases and the peaks are relatively weak compared to the peaks from the C_p profiles. The C_p and $C_p + 2\overline{v'^2}/u_\infty^2$ become almost identical for $y/d > 4$ which seems to indicate the inviscid flow region.

To clarify the inviscid flow region, we investigate the distribution of the mean total pressure coefficient (C_{pt}) in figure 3.4(d-f). The total pressure coefficient can be written as

$$C_{pt} = \frac{\bar{p} + \frac{1}{2}\rho(\bar{u}^2 + \bar{v}^2 + \bar{u}'^2 + \bar{v}'^2 + \bar{w}'^2) - p_\infty - \frac{1}{2}\rho u_\infty^2}{\frac{1}{2}\rho u_\infty^2}. \quad (3.19)$$

$C_{pt} = 0$ indicates that the flow is governed by the potential theory. The y/d for $C_{pt} = 0$ almost coincides with y/d for negligible $\overline{v'^2}/u_\infty^2$ (figure 3.4a-f). Therefore, \bar{p}_o should be the pressure at y/d where C_{pt} becomes zero. Then, we can divide the outlet of the control volume into the wake region and the inviscid flow region based on the total pressure coefficient (figure 3.4d-f).

Figure 3.4(g-i) show the mean streamwise velocity deficits. The velocity deficits decrease in the wake region and become negative (figure 3.4d-i). As y/d increases further, the velocity deficits approach to zero (figure 3.4g-i). Therefore, we modeled $\bar{p}_o(x)$ as the pressure at the y/d where the maximum mean streamwise velocity (u_{max}) is observed.

The drag coefficients, predicted by the present model, are compared with the numerical ones in figure 3.4, together with those predicted by the models of Dimotakis (1977) and Antonia & Rajagopalan (1990). The

original formulation suggested by Dimotakis (1977) is expressed as

$$C_D = \frac{2}{d(1 - \delta_1/H)^2} \left\{ \int_{-H/2}^{H/2} \left(\frac{\bar{u}}{\bar{u}_e} \left(1 - \frac{\bar{u}}{\bar{u}_e} \right) + \frac{\bar{v}^2 + \bar{v}'^2 - \bar{u}'^2}{\bar{u}_e^2} \right) dy + \frac{\delta_1^2}{2H} \right\}, \quad (3.20)$$

where $\bar{u}_e = \bar{u}_{y=H/2}$ and

$$\delta_1 = \int_{-H/2}^{H/2} \left(1 - \frac{\bar{u}}{\bar{u}_e} \right) dy. \quad (3.21)$$

We can interpret the present model as the model by Antonia & Rajagopalan (1990) with an additional correction term. The predicted drag coefficients without the correction term are largely underestimated. The main cause of the underestimation is that one cannot consider the effect of the non-zero pressure coefficient in the inviscid flow (figure 3.4a-c) without the correction term. The model of Dimotakis (1977) considers the effect of the non-zero pressure coefficient in the inviscid flow but it neglects the effect of the non-uniform pressure distribution in the inviscid flow which results in large errors. The present model shows much better prediction performance compared to the previous models (Dimotakis 1977; Antonia & Rajagopalan 1990) by considering a criterion for the boundary between the wake and the inviscid flow (figure 3.4). Although the present model is investigated for $x/d \leq 10$, the extension to the far wake is straightforward. The Reynolds normal stress terms can be neglected as in many textbooks (Tennekes & Lumley 1972; Pope 2000) but the additional correction term in (3.14) might be included for the infinite integration range since the term can explain the effect of the change in governing equations along transverse direction.

3.3. Criteria for the accurate prediction

The performance of the present model (3.14) depends on the choices of the integral height (H) and streamwise measurement location (x_m). As H and x_m increase, the performance should be better. Hence, it is important to see how the drag coefficient varies with H and x_m for various Reynolds numbers, and to determine minimum H and x_m for the accurate prediction of the drag coefficient.

The drag coefficients predicted by Eq. (3.14), normalized by the ones ($C_{D,CFD}$) directly obtained from the present simulations, are shown in Fig. 3.5 by varying x_m while keeping $H = L_y$ (the size of the integral height is equal to the computational domain size). Here, the drag coefficients predicted by Eqs. (3.17) and (3.16) are also drawn for comparison at $Re = 3900$ and 250000 . The drag coefficient predicted by the present model approaches $C_{D,CFD}$ with increasing x_m . On the other hand, the drag coefficients predicted by Eqs. (3.17) and (3.16) are much smaller than $C_{D,CFD}$ (even becoming negative) even at large x_m . This better performance of the present model comes from the inclusion of the second term on the right hand side of Eq. (3.14). When x_m/d is small, all the models show large errors because the streamwise gradients of the velocity statistics are non-negligible in the near wake.

Since the converged C_D occurs at different x_m 's for different Re 's, we suggest a new normalized measurement location, at which C_D 's converge for different Reynolds numbers. Since the flow in the near-wake region is dominated by the vortex shedding, one of the important length scales in the wake is the vortex formation length, so that we introduce x_{vm} at which $\overline{v'^2}$ on the centerline is maximum. Another important length scale is the wake half width $y_{1/2}$ where $u_\infty - \overline{u}_{y=y_{1/2}} = 0.5(u_\infty - \overline{u}_{y=0})$.

With these length scales, we plot $C_D/C_{D,CFD}$ vs. $(x_m - x_{vm})/y_{1/2}$ in Fig. 3.5(b). As shown, the scattering of the curves along x_m is much less with this normalization. We suggest that $(x_m - x_{vm})/y_{1/2} = 10$ should be enough to accurately predict the drag coefficient.

Fig. 3.6(a) shows the variations of the predicted drag coefficient with the integral height H at $(x_m - x_{vm})/y_{1/2} = 10$, together with those predicted by Eqs. (3.17) and (3.16). As H increases, the drag coefficients predicted by the present model increase and converge at $H/d > 6.3$ and 6.0 for $Re = 3900$ and 250000 , respectively. Note that the mean streamwise velocities at these x_m 's are maximum (u_o) at $y_o/d = 3.8$ and 3.4 for these Reynolds numbers, respectively, and thus the integral height should be $H \gtrsim 2y_o$ for the accurate estimation of the drag coefficient. On the other hand, the drag coefficients predicted by Eqs. (3.16) and (3.17) first increase and then decrease with increasing H , indicating that the inclusion of the inviscid flow region in Eq. (3.14) is important. Note that $y_1/d = 2.1$ at $Re = 3900$ and Eq. (3.17) becomes the maximum at $H = 2y_1$ since the contribution from the mean streamwise velocity is negative and dominant for $|y| > y_1$. However, the predicted drag coefficient by Eq. (3.17) is underestimated even at its maximum. Note also that Eq. (3.16) predicts the drag coefficient quite accurately only when $H \approx 2y_o$, but a further increase in the integral height decreases the drag coefficient, showing an inconsistency in the prediction and thus $H \approx 2y_o$ should be adopted for Eq. (3.16) as we mentioned earlier. The low sensitivity of H near $H = 2y_o$ on the predicted drag coefficient by Eq. (3.16) comes from the small difference between \bar{u} and u_o and the negligible velocity fluctuations near $y = y_o$. The difference between the predicted drag coefficients by Eqs. (3.16) and (3.14) is also negligible for $H \approx 2y_o$. Fig. 3.6(b) shows

the variation of the predicted drag coefficient with $H/y_{1/2}$ for five different Reynolds numbers. $H/y_{1/2}$ provides a better normalization since five curves collapse slightly better than H/d . At $H/y_{1/2} \geq 10$, the drag coefficient converges for all the Reynolds numbers.

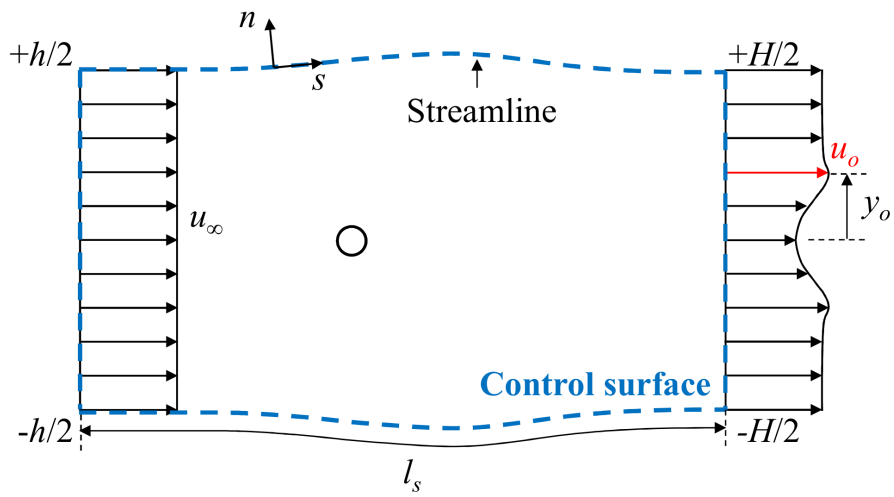


FIGURE 3.1. Schematic diagram of the control volume analysis.

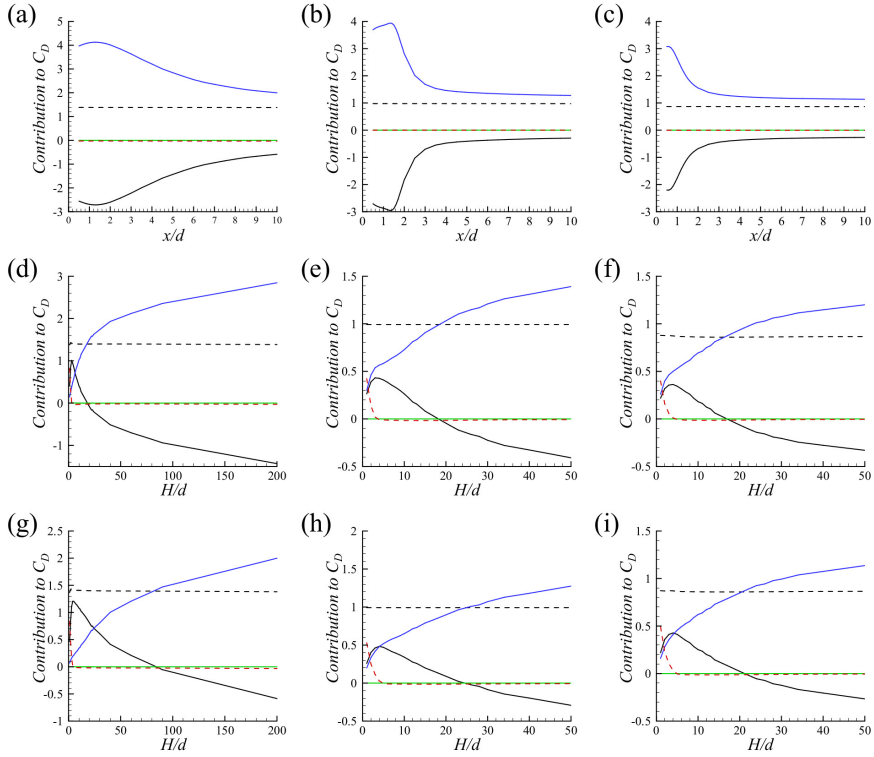


FIGURE 3.2. Contribution to C_D from each term in (3.18): with integration range equal to the domain size; (a) $Re = 50$; (b) 3900; (c) 250000; at $x/d = 5$; (d) $Re = 50$; (e) 3900; (f) 250000; at $x/d = 10$ (g) $Re = 50$; (h) 3900; (i) 250000. Black dashed line, C_D ; black solid line, contribution from convective flux at the outlet; blue solid line, contribution from the pressure at the outlet; green solid line, contribution from the viscous diffusion at the outlet; red dashed line, contribution from the pressure and the viscous diffusion at the streamline.

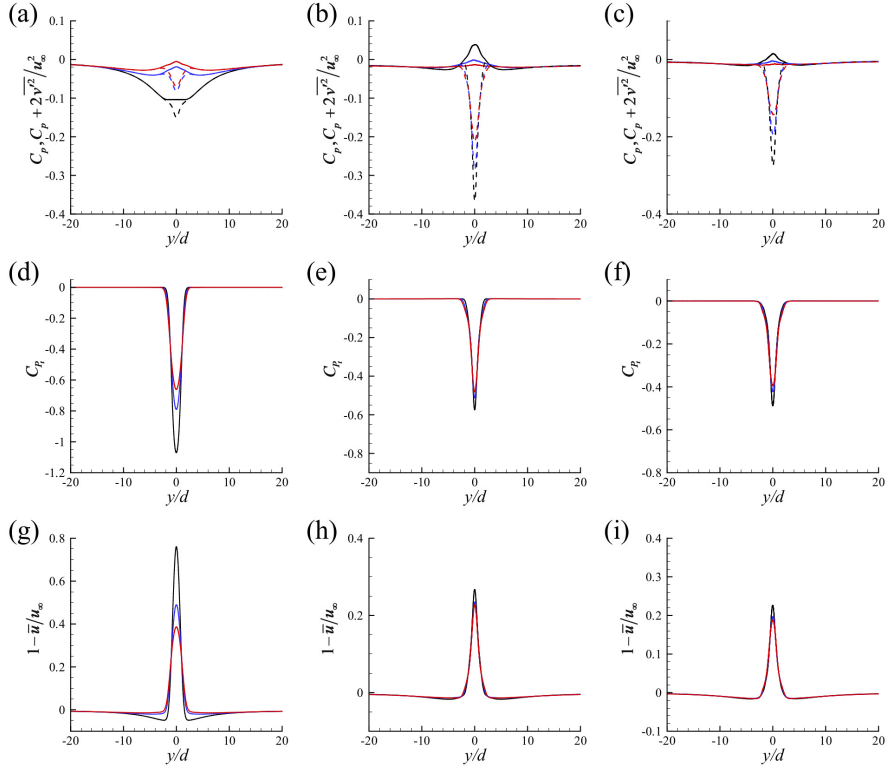


FIGURE 3.3. Pressure coefficients (C_p) and effects of the pressure coefficient estimation ($C_p + 2\overline{v^2}/u_\infty^2$): (a) $Re = 50$; (b) 3900; (c) 250000. Total pressure coefficients (C_{P_t}): (d) $Re = 50$; (e) 3900; (f) 250000. The mean streamwise velocity deficits ($1 - \bar{u}/u_\infty$): (g) $Re = 50$; (h) 3900; (i) 250000. Black line, $x/d = 5$; blue line, $x/d = 7.5$; red line, $x/d = 10$. In (a), (b) and (c), solid line, $C_p + 2\overline{v^2}/u_\infty^2$; dashed line, C_p .

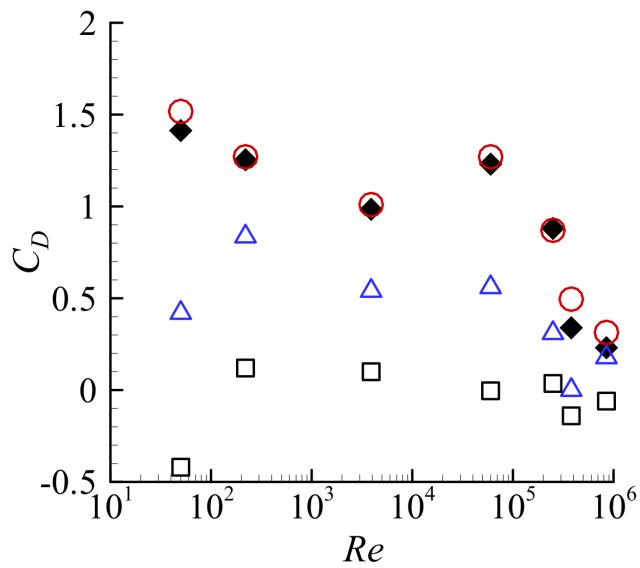


FIGURE 3.4. Measured and predicted drag coefficients at $x/d = 10$. \blacklozenge , $C_{D,CFD}$; \circ , present; \triangle , Dimotakis (1977); \square , Antonia & Rajagopalan (1990).

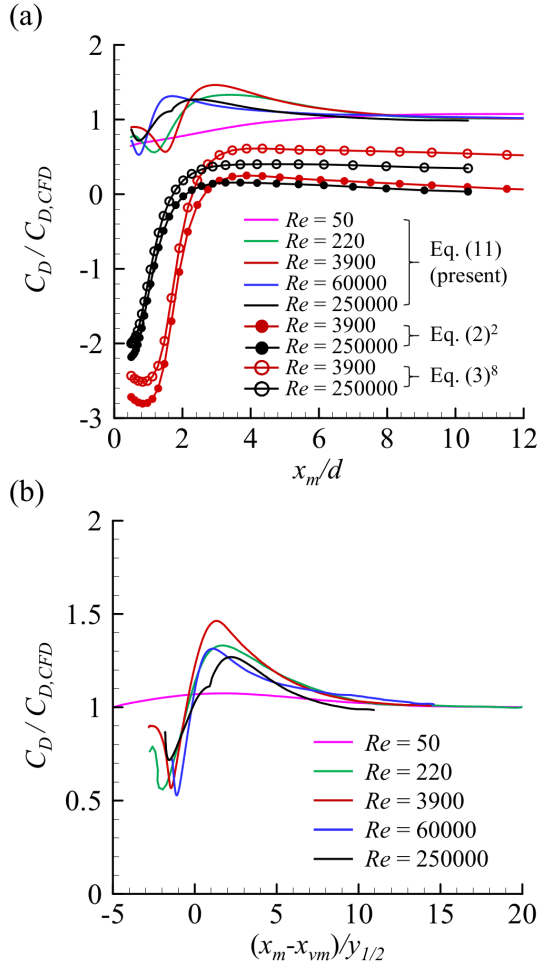


FIGURE 3.5. Variations of the drag coefficient predicted by the present model with x_m ($H = L_y$): (a) $C_D / C_{D,CFD}$ vs. x_m / d ; (b) $C_D / C_{D,CFD}$ vs. $(x_m - x_{vm}) / y_{1/2}$.

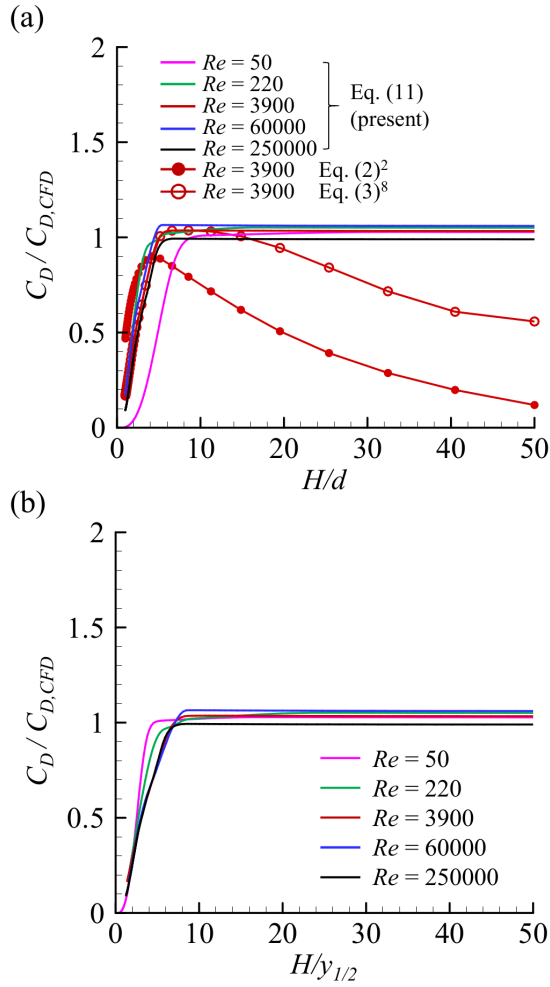


FIGURE 3.6. Variations of the drag coefficient predicted by the present model with H ($(x_m - x_{vm})/y_{1/2} = 10$): (a) $C_D/C_{D,CFD}$ vs. H/d ; (b) $C_D/C_{D,CFD}$ vs. $H/y_{1/2}$.

Chapter 4

Universal Strouhal number and a scaling law regarding the drag

4.1. Characteristic scales for the vortex formation

Previous researchers have suggested the characteristic velocity scale as $u_b = u_\infty \sqrt{1 - C_{pb}}$ (Roshko 1954; Calvert 1967; Simmons 1977; Griffin 1978; Rodríguez *et al.* 2015). They proposed a physical meaning for this velocity as the approximation of the mean velocity at the edge of the boundary layer of the separation point. Figure 4.1 shows the comparison of the normalized azimuthal velocity and velocity magnitude with the base pressure parameter, $K = \sqrt{(1 - C_{pb})}$, showing the validity of this meaning. At a low Reynolds number ($Re = 50$), the boundary layer at the separation point is so thick that the angular difference between the azimuthal direction and streamline outside the boundary layer is large. Therefore, it is a reasonable choice to compare the K with $|\bar{\mathbf{u}}_{sep}|/u_\infty$ than with $\bar{u}_{\theta,sep}/u_\infty$. K and $|\bar{\mathbf{u}}_{sep}|/u_\infty$ are quite similar except at the critical Reynolds numbers. At the critical Reynolds numbers, the base-pressure parameter decreases as the Reynolds number increases while $|\bar{\mathbf{u}}_{sep}|/u_\infty$

increases as the Reynolds number increases. It might be related to the boundary layer transition which occurs at the critical regime. At the super-critical Reynolds number, K is the same with $|\bar{\mathbf{u}}_{sep}|/u_\infty$ at the turbulent separation point (main separation). Therefore, the physical meaning suggested is not universal. However, Rodríguez *et al.* (2015) showed that this velocity scale showed good performance for obtaining a universal Strouhal number even at the critical regimes. Therefore, another physical explanation is necessary or a better velocity scale should be proposed.

We suggest wake coordinates from the mean flow fields as the characteristic scales at the vortex formation region. Figure 4.2 shows the wake coordinates along the streamwise direction where $\bar{u}_d = u_\infty - \bar{u}$ and $y_{1/2}$ is defined as $\bar{u}_d(y = y_{1/2}) = \frac{1}{2}\bar{u}_d(y = 0)$. From figure 4.2(a-b), the minimum of the wake half-width and the maximum of the wake deficit is observed inside the recirculation region. Note that the end of the recirculation region is $x/d = 2.1$ ($\bar{u}_{dc}/u_\infty = 1$). The maximum of the wake deficit occurs at the upstream from the minimum of the wake half-width. Figure 4.2(c) represents the wake deficit divided by the half-width normalized by u_∞ and d . Assuming the self-similarity of the mean streamwise velocity deficit in the vortex formation region, this parameter is proportional to the mean shear rate at each streamwise location. From a turbulent channel flow study by Lozano-Durán & Bae (2019), the characteristic time of the momentum-carrying eddies scales with inverse of the mean shear rate. Therefore, we propose an assumption that the time scale of the Karman vortex shedding proportional to the inverse of the maximum of $\bar{u}_{dc}/y_{1/2}$ which means the universal Strouhal number can be written as $f y_{1/2}/\bar{u}_{dc}$.

To compare the performance of the proposed scales, the Strouhal numbers defined with the various length and velocity scales are plotted in fig-

ure 4.3. The conventional Strouhal number is shown with open circle symbol and the maximum of the value is 268% larger than the minimum of the value. d_{uu} represents the transverse distance between the maximum RMS of the streamwise velocity at the streamwise location where the transverse distance becomes minimum which is the definition of the wake width used in Griffin (1978); Rodríguez *et al.* (2015). d_{up} represents the transverse distance between the maximum RMS of the streamwise velocity at the streamwise location where the mean pressure along the streamline is the minimum. fd_{uu}/u_b and fd_{up}/u_b are shown with the blue triangle and the green square, respectively, and the maximum of each value is 46% and 86% larger than the minimum of each value, respectively. The universal Strouhal numbers suggested in this study, $\frac{f}{\bar{u}_{dc}/y_{1/2}|_{max}}$, show much less variation than those from the other studies. The maximum of the value is only 16% larger than the minimum of the value suggesting independence on the Reynolds number.

Figure 4.4 shows the streamwise location of each formation origin depending on the Reynolds number, where x_{uu} , x_{up} and x_{dm} represent the streamwise location where we get d_{uu} , d_{up} and $y_{1/2}$ at the above paragraph, respectively. For all the definitions of the formation origin, the streamwise location does not show a linear relationship with the Reynolds number. The x_{dm}/d is the largest at $Re = 3900$ among all the Reynolds numbers in the present study. At $Re = 50$, the difference among the formation origin is large. x_{dm} is always located inside the recirculation region but x_{uu} at $Re = 50, 380000$ and 850000 locates downstream of the recirculation region (not shown in the figure).

4.2. A scaling law for the drag of two-dimensional bluff bodies

To investigate the relation between the drag of the body and the characteristic scales of the wake, we conduct a budget analysis of the drag coefficient in this section. A formulation for the drag coefficient which is the integral form of the flow variables is needed. From the control volume analysis in chapter 3, (3.8) can be rewritten as,

$$C_D = \frac{2}{d} \int_{-\frac{H}{2}}^{\frac{H}{2}} \left(\bar{u} - \frac{\bar{u}^2}{u_\infty^2} \right) dy - \frac{2}{d} \int_{-\frac{H}{2}}^{\frac{H}{2}} \frac{\overline{u'^2}}{u_\infty^2} dy - \frac{1}{d} \int_{-\frac{H}{2}}^{\frac{H}{2}} C_p dy. \quad (4.1)$$

However, this formulation has a disadvantage that it highly depends on the size of the inviscid flow region which is not a region of interest in this section. Therefore, a new formulation using the total pressure instead of the static pressure is introduced in this section. Also, instead of the streamwise velocity, the velocity deficit ($u_d \equiv u_\infty - u$) should be used for the new formulation. Then, (4.1) becomes

$$C_D = \frac{2}{d} \int_{-\frac{H}{2}}^{\frac{H}{2}} \left(-\frac{\bar{u}_d^2}{u_\infty^2} + \frac{\bar{v}^2}{u_\infty^2} \right) dy + \frac{2}{d} \int_{-\frac{H}{2}}^{\frac{H}{2}} \left(-\frac{\overline{u'^2}}{u_\infty^2} + \frac{\overline{v'^2}}{u_\infty^2} + \frac{\overline{w'^2}}{u_\infty^2} \right) dy - \frac{1}{d} \int_{-\frac{H}{2}}^{\frac{H}{2}} C_{pt} dy. \quad (4.2)$$

The first, second and the third integral in (4.1) represent the contributions of the mean velocity, the fluctuation velocity and the static pressure, respectively. Those in (4.2) represent the contributions of the mean velocity, the fluctuation velocity and the total pressure, respectively, similar to (4.1). The streamwise velocity components are only used for the integral in (4.1), while the transverse and the spanwise velocity components are also used for all the integral in (4.2) due to the definition of the total pressure. In (4.2), streamwise velocity components in the first and the

second integrals always give negative contribution to the drag coefficient. The figure 4.5 shows the budgets for the drag coefficient at the formation origin (x_{dm}) for $Re = 3900$. At $H/d \approx 4$, the drag coefficient converges to the $C_{D,CFD}$. In the figure 4.5(a), the contribution from the streamwise velocity fluctuations also converges at $H/d \approx 4$ but the contributions from the others do not converge and their magnitudes increase as H/d increases. However, in the formulation based on the velocity deficit and the total pressure, all the integrals converge at $H/d \approx 4$. The contributions from the total pressure and the velocity fluctuation are positive while that from the mean velocity is negative at x_{dm} . The contribution from the velocity fluctuation is much smaller than the contribution from the others.

Based on the fact that the total pressure term in (4.2) is the largest, the effect of the total pressure should not be neglected in estimating the drag. Therefore, the characteristic scale for the total pressure is essential to scale the drag based on the parameters in the wake. For the characteristic scale for the total pressure, we propose a total pressure deficit at the centerline ($\bar{p}_{tdc} \equiv p_{t,\infty} - \bar{p}_{tc}$) at x_{dm} . Then, with the characteristic length and velocity scales for the Karman vortex formation from the previous section, we may model the drag coefficient at x_{dm} (x at $\bar{u}_{dc}/y_{1/2}|_{max}$) as,

$$C_D \approx \alpha \frac{\bar{u}_{dc}^2}{u_\infty^2} \frac{y_{1/2}}{d} + \beta \frac{\bar{p}_{tdc}}{\frac{1}{2}\rho u_\infty^2} \frac{y_{1/2}}{d}, \quad (4.3)$$

where α and β denote empirical parameters which are constant. Since the normalized total pressure deficit represents the minus of the total pressure coefficients, (4.3) can be written as,

$$C_D \approx \alpha \frac{\bar{u}_{dc}^2}{u_\infty^2} \frac{y_{1/2}}{d} - \beta C_{p_{tc}} \frac{y_{1/2}}{d}. \quad (4.4)$$

The first term on the right hand side of (4.4) represents the modeling of the contribution from the velocity deficit in (4.2) which can be written as,

$$\alpha \frac{\bar{u}_{dc}^2}{u_\infty^2} \frac{y_{1/2}}{d} \approx \frac{1}{d} \int_{-\frac{H}{2}}^{\frac{H}{2}} -\frac{\bar{u}_{dc}^2}{u_\infty^2} dy, \quad (4.5)$$

for H goes to ∞ , and $H = L_y$ in a practical sense. Based on a theoretical solution for the far wake with constant turbulent viscosity, the mean streamwise velocity deficit ($\bar{u}_{d,theory}$) becomes,

$$\frac{\bar{u}_{d,theory}}{u_\infty} = \frac{\bar{u}_{dc}}{u_\infty} \exp^{-\ln 2 \left(\frac{y_{1/2}}{d} \right)^2}. \quad (4.6)$$

By substituting (4.6) into (4.4), we can obtain the theoretical value of the empirical constant ($\alpha_{theory} = -1.505$). Figure 4.6(a) compares the the contribution from the velocity deficit in (4.2) with the first term in (4.4) using α_{theory} and it indicates the theoretical approximation agrees well with the simulation results. Figure 4.6(b) represents the α directly obtained by substituting the simulation results into (4.5). The measured α is slightly lower than the theoretical value and the averaged value for the all the Reynolds numbers is -1.58.

For the second term on the right hand side of (4.4), we suggest a rough estimate that the term can approximate the contribution from all the terms except the term regarding the mean velocity deficit. Figure 4.7 shows $C_D + \frac{1}{d} \int_{-\frac{H}{2}}^{\frac{H}{2}} -\frac{\bar{u}_{dc}^2}{u_\infty^2} dy$ versus $C_{ptc} \frac{y_{1/2}}{d}$ to check the validity of the estimation. The slope of the linear fitting line represents the mean value of β based on our simulation results which is 2.78. Using the empirical constants (α, β) from our simulation results, the drag coefficient model can be obtained with the characteristic length, velocity and total pressure

scales at the streamwise location where $\bar{u}_{dc}/y_{1/2}$ is maximum as,

$$C_{D,model} = -1.58 \frac{\bar{u}_{dc}^2}{u_\infty^2} \frac{y_{1/2}}{d} - 2.78 C_{ptc} \frac{y_{1/2}}{d}. \quad (4.7)$$

The drag coefficients predicted by the characteristic length, velocity and total pressure scales show excellent agreements with those by numerical simulations (figure 4.8).

Now, we are going to derive a scaling law regarding C_D , St and C_{pb} based on the model derived in (4.7). From the definition of the universal Strouhal number suggested in the present study in the previous section ($St_{univ} \equiv \frac{f y_{1/2}}{\bar{u}_{dc}}$ at x_{dm}), we can eliminate $y_{1/2}$ in (4.7) by substituting $y_{1/2} = d \frac{1}{St} \frac{\bar{u}_{dc}}{u_\infty}$. Then the drag coefficient can be scaled as,

$$C_D \sim -1.58 \frac{\bar{u}_{dc}^3}{u_\infty^3} \frac{1}{St} - 2.78 C_{ptc} \frac{\bar{u}_{dc}}{u_\infty} \frac{1}{St}. \quad (4.8)$$

Figure 4.9(a) shows the \bar{u}_{dc}/u_∞ depending on the Reynolds number. The \bar{u}_{dc}/u_∞ is almost constant regardless of the Reynolds number and the averaged value from the present data is 1.17. Then, by assuming constant value of \bar{u}_{dc}/u_∞ (=1.17), the drag coefficient can be scaled as,

$$C_D \sim \frac{1}{St} (-0.78 - C_{ptc}). \quad (4.9)$$

Figure 4.9(b) shows $-C_{ptc}$ versus $1 - C_{pb}$. Since the x_{dm} locates close to the body and inside the recirculation region, $-C_{ptc} \sim 1 - C_{pb}$. Then, we can obtain a scaling law regarding C_D , St and C_{pb} as,

$$C_D \sim \frac{1}{St} (0.22 - C_{pb}). \quad (4.10)$$

To check the validity of the scaling law, we compare the C_D with $\frac{1}{St} (0.22 - C_{pb})$ in figure 4.10(a). Not only the data from present simulation but also those from other two-dimensional bluff bodies (Mariotti

et al. 2019; Cao *et al.* 2020) are plotted and the scaling law seems to be valid regardless of the body shape and the Reynolds number. To investigate the effectiveness of the present scaling law, we compare the drag coefficient and the drag coefficient divided by (4.10) in figure 4.10(b). The maximum difference of the drag coefficient considered in the scaling law is about 1000%, while that of the scaled drag coefficient is only about 60%.

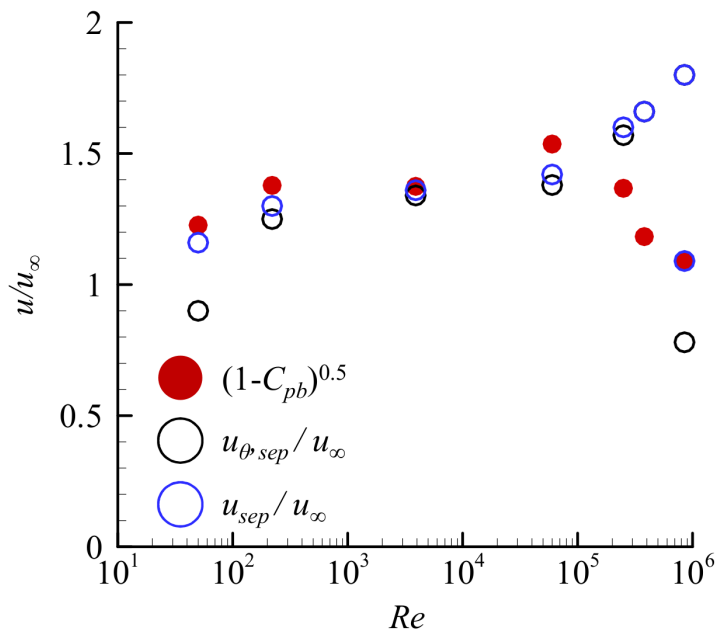


FIGURE 4.1. Comparison for characteristic velocity scales.

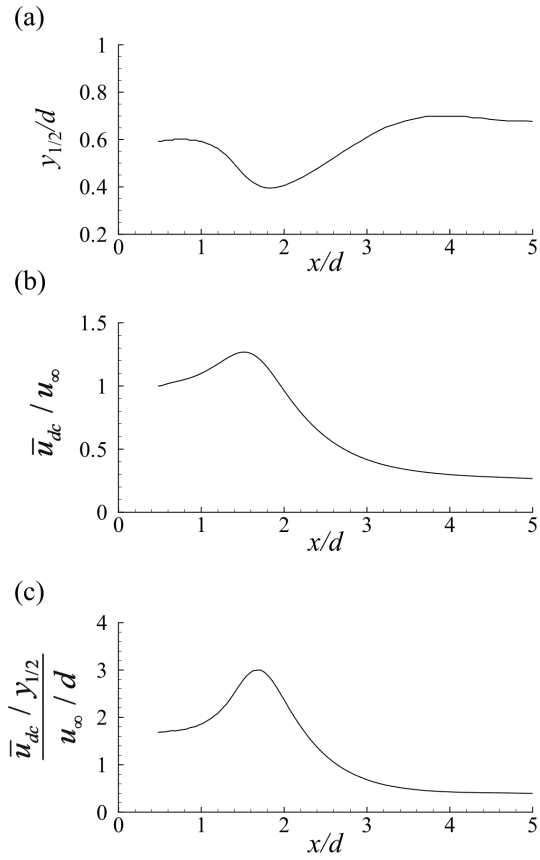


FIGURE 4.2. Wake coordinate statistics along the centerline at $Re = 3900$: (a) half width ($y_{1/2}/d$); (b) mean velocity deficit

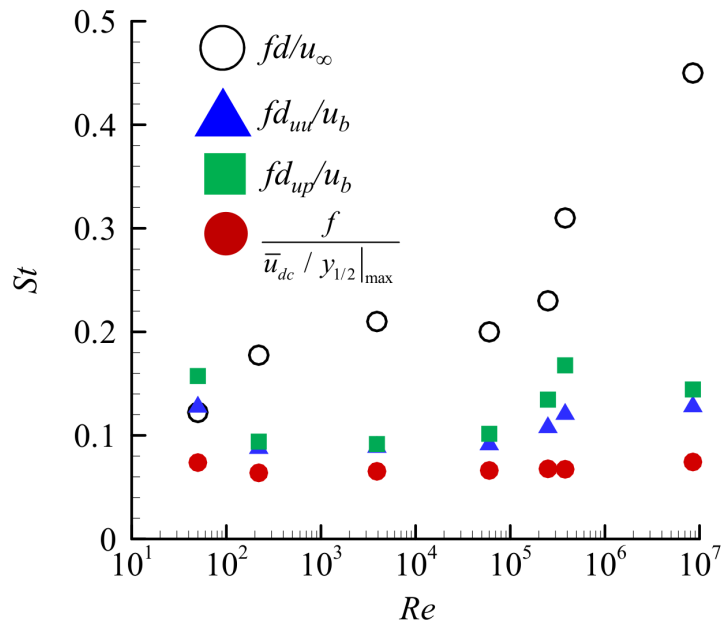


FIGURE 4.3. Comparison of the universal Strouhal numbers.

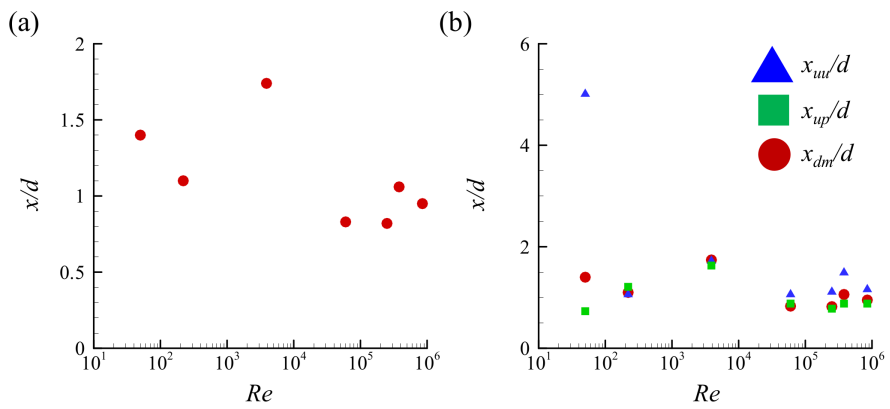


FIGURE 4.4. Streamwise location for the vortex formation origin: (a) present suggestion; (b) present suggestion compared with other studies.

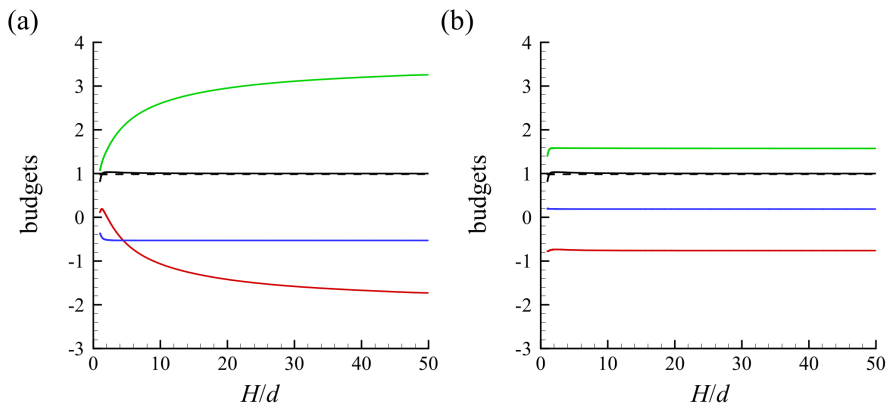


FIGURE 4.5. Budget analysis for the drag coefficient at $x = x_{dm}$ for $Re = 3900$: (a) conventional formulation; (b) velocity deficit and total pressure based formulation. Red line, mean velocity; blue line, Reynolds stress; green line, pressure (static or total); black line, sum of the budgets; dashed line, $C_{D,CFD}$.

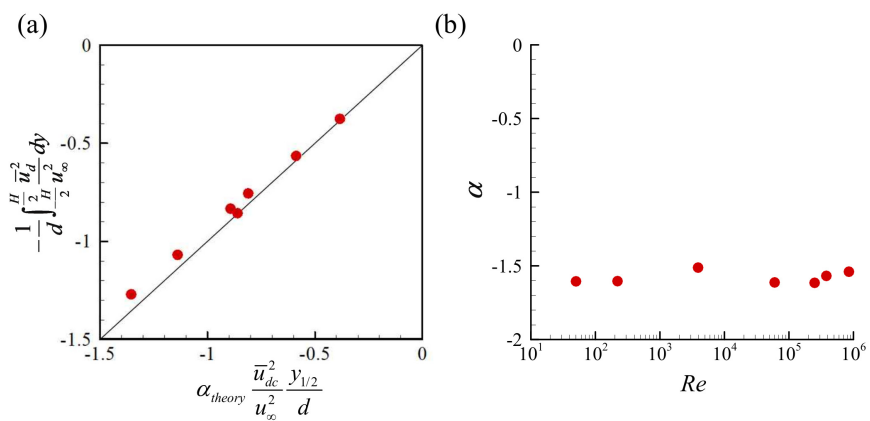


FIGURE 4.6. (a) Comparison between $\alpha_{theory} \frac{\bar{u}_{dc}^2}{u_\infty^2} \frac{y_{1/2}}{d}$ and $\frac{1}{d} \int_{-\frac{H}{2}}^{\frac{H}{2}} -\frac{\bar{u}_d^2}{u_\infty^2} dy$; (b) measured α .

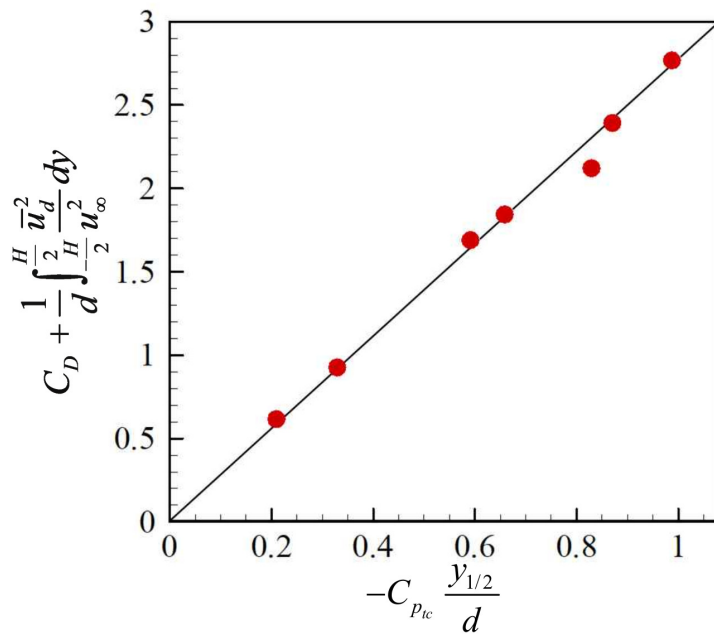


FIGURE 4.7. $C_D + \frac{1}{d} \int_{-\frac{H}{2}}^{\frac{H}{2}} \frac{\bar{u}_d^2}{u_\infty^2} dy$ versus $C_{p,c} \frac{y_{1/2}}{d}$.

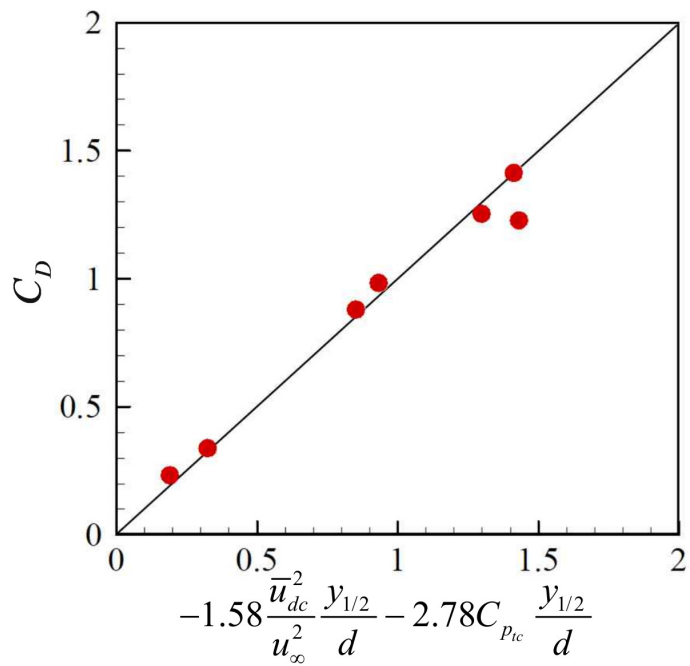


FIGURE 4.8. C_D from the simulation versus C_D from modeling based on the characteristic scales at x_{dm} .

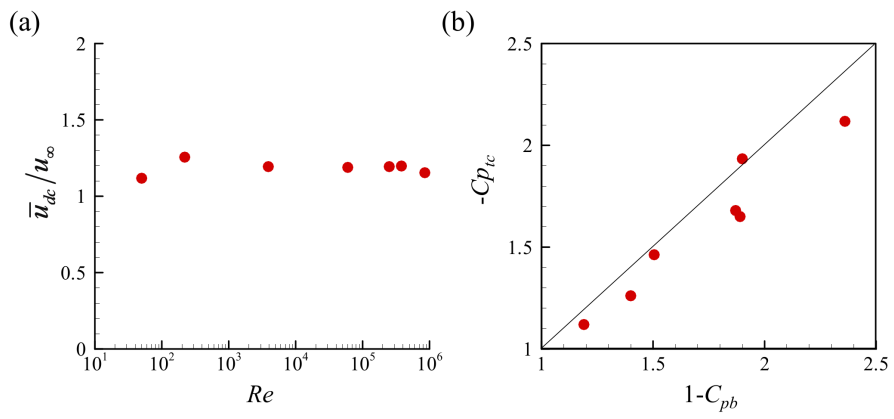


FIGURE 4.9. (a) \bar{u}_{dc}/u_∞ versus Re ; (b) $-C_{p_{tc}}$ versus $1 - C_{pb}$ at x_{dm} .

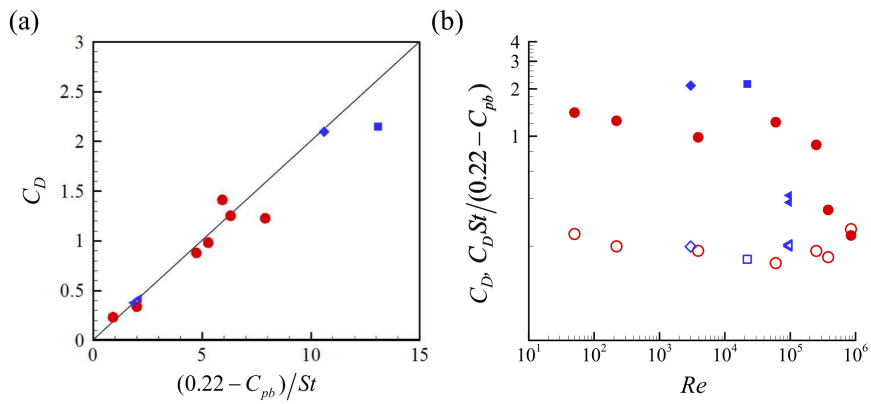


FIGURE 4.10. The performance of the scaling law regarding C_D , St and C_{pb} : (a) C_D versus $(0.22 - C_{pb})/St$; (b) C_D and $C_D St / (0.22 - C_{pb})$ depending on the Re . Solid and open symbols represent C_D and $C_D St / (0.22 - C_{pb})$, respectively and \circ , present; \diamond , flat plate at $Re = 3000$, \square , square prism at $Re = 22000$ (Cao *et al.* 2020) \triangleleft , boat-tailed bluff body at $Re = 96000$ (Mariotti *et al.* 2019).

Chapter 5

Conclusions

In the present study, we proposed an improved prediction model of the mean drag coefficient from the mean streamwise velocity and the Reynolds normal stresses at a streamwise location in the near wake of a circular cylinder. We conducted a control volume analysis to get the relation between the drag coefficient and the flow fields. The contribution to C_D from each term was analyzed based on the present simulation results. Neglecting viscous effects and the contributions from the pressure at the streamline were seemed to be reasonable considering sufficiently high Reynolds number and wide integration range. To model the contribution from the pressure distribution at the outlet, we divided the outlet into the wake region and the inviscid flow region based on the mean streamwise velocity profile and adopted the boundary layer approximation and the Bernoulli equation, respectively. The drag coefficients predicted by the present model agreed well with those from present numerical simulation while those predicted by the previous models (Dimotakis 1977; Antonia & Rajagopalan 1990) showed significant errors with the wide integration

range.

We also suggested another drag prediction model based on the characteristic scales which were proposed to explain the universality of the Karman vortex formation. The characteristic scales were the mean velocity deficit on the centerline, the half-width of wake and the mean total pressure deficit on the centerline obtained at a streamwise location where the mean velocity deficit divided by the half-width became maximum. Based on these scales, we proposed not only a drag prediction model but also a universal Strouhal number. Also, with additional assumptions validated by the present simulation results, we derived a scaling law regarding the relation among the drag coefficient, Strouhal number and the base pressure coefficient. Data from other two-dimensional bodies agreed well with the present scaling law.

References

- ACHENBACH, E 1968 Distribution of local pressure and skin friction around a circular cylinder in cross-flow up to $re = 5 \times 10^6$. *Journal of Fluid Mechanics* **34** (4), 625–639.
- ACHENBACH, E. & HEINECKE, E. 1981 On vortex shedding from smooth and rough cylinders in the range of reynolds numbers 6×10^3 to 5×10^6 . *Journal of fluid mechanics* **109**, 239–251.
- ADACHI, TSUTOMU 1995 The effect of surface roughness of a body in the high reynolds-number flow. *International Journal* **2** (1), 23–32.
- AHMED, NA & WAGNER, DJ 2003 Vortex shedding and transition frequencies associated with flow around a circular cylinder. *AIAA journal* **41** (3), 542–544.
- ANTONIA, R.A. & RAJAGOPALAN, S. 1990 Determination of drag of a circular cylinder. *AIAA journal* **28** (10), 1833–1834.
- BEARMAN, PETER W 1969 On vortex shedding from a circular cylinder in the critical reynolds number regime. *Journal of Fluid Mechanics* **37** (3), 577–585.
- BEAUDAN, P. & MOIN, P. 1994 Numerical experiments on the flow past a circular cylinder at sub-critical reynolds number. *Tech. Rep.*. Stanford Univ CA Thermosciences Div.
- BHATTACHARYA, S. & GREGORY, J.W. 2015 Effect of three-dimensional plasma

- actuation on the wake of a circular cylinder. *AIAA Journal* **53** (4), 958–967.
- BLOOR, M SUSAN 1964 The transition to turbulence in the wake of a circular cylinder. *Journal of Fluid Mechanics* **19** (2), 290–304.
- CADOT, O., DESAI, A., MITTAL, S., SAXENA, S. & CHANDRA, B. 2015 Statistics and dynamics of the boundary layer reattachments during the drag crisis transitions of a circular cylinder. *Physics of Fluids* **27** (1), 014101.
- CALVERT, JR 1967 Experiments on the low-speed flow past cones. *Journal of Fluid Mechanics* **27** (2), 273–289.
- CANTWELL, BRIAN & COLES, DONALD 1983 An experimental study of entrainment and transport in the turbulent near wake of a circular cylinder. *Journal of fluid mechanics* **136**, 321–374.
- CAO, YONG, TAMURA, TETSURO & KAWAI, HIDENORI 2020 Spanwise resolution requirements for the simulation of high-reynolds-number flows past a square cylinder. *Computers & Fluids* **196**, 104320.
- CAPONE, ALESSANDRO, KLEIN, CHRISTIAN, DI FELICE, FABIO & MIOZZI, MASSIMO 2016 Phenomenology of a flow around a circular cylinder at sub-critical and critical reynolds numbers. *Physics of Fluids* **28** (7), 074101.
- CHENG, WAN, PULLIN, DI, SAMTANEY, RAVI, ZHANG, W & GAO, WEI 2017 Large-eddy simulation of flow over a cylinder with from to: a skin-friction perspective. *Journal of Fluid Mechanics* **820**, 121–158.
- CHOI, H. & MOIN, P. 1994 Effects of the computational time step on numerical solutions of turbulent flow. *Journal of Computational Physics* **113** (1), 1–4.
- DIMOTAKIS, P.E. 1977 Laser doppler velocimetry momentum defect measurements of cable drag at low to moderate reynolds numbers: feasibility study. *Tech. Rep.* N62583/77 - M - RS41. Naval Construction Battalion Center.
- DONG, SUCHUAN & KARNIADAKIS, GEORGE E 2005 Dns of flow past a stationary and oscillating cylinder at $re= 10000$. *Journal of fluids and structures* **20** (4), 519–531.

- FARELL, C & BLESSMANN, J 1983 On critical flow around smooth circular cylinders. *Journal of Fluid Mechanics* **136**, 375–391.
- FENG, L.-H. & WANG, J.-J. 2014 The virtual aeroshaping enhancement by synthetic jets with variable suction and blowing cycles. *Physics of Fluids* **26** (1), 014105.
- GRIFFIN, OWEN M 1978 A universal strouhal number for the ‘locking-on’ of vortex shedding to the vibrations of bluff cylinders. *Journal of Fluid Mechanics* **85** (3), 591–606.
- GRIFFIN, OWEN M 1980 Universal similarity in the wakes of stationary and vibrating bluff structures. In *Wind Engineering*, pp. 607–617. Elsevier.
- HAMED, A.M., VEGA, J., LIU, B. & CHAMORRO, L.P. 2017 Flow around a semicircular cylinder with passive flow control mechanisms. *Experiments in Fluids* **58** (3), 22.
- HENDERSON, R.D. 1995 Details of the drag curve near the onset of vortex shedding. *Physics of Fluids* **7** (9), 2102–2104.
- IBRAHIM, AHMED, HUANG, CHEN-PEY, KORPUS, RICHARD & DALTON, CHARLES 2016 Cfd simulation of current past bluff body at high reynolds number. In *Offshore Technology Conference*. OnePetro.
- KIM, J. & CHOI, H. 2005 Distributed forcing of flow over a circular cylinder. *Physics of Fluids* **17** (3), 033103.
- KIM, J., KIM, D. & CHOI, H. 2001 An immersed-boundary finite-volume method for simulations of flow in complex geometries. *Journal of computational physics* **171** (1), 132–150.
- KIM, K., BAEK, S.-J. & SUNG, H. 2002 An implicit velocity decoupling procedure for the incompressible navier–stokes equations. *International journal for numerical methods in fluids* **38** (2), 125–138.
- KIM, N., KIM, H. & PARK, H. 2015 An experimental study on the effects of rough hydrophobic surfaces on the flow around a circular cylinder. *Physics of Fluids* **27** (8), 085113.
- KIM, SUNGWOOK, CHOI, HAECHON & YOO, JUNG YUL 2007 Effect of local

- forcing on backward-facing step flow with laminar separation. *Journal of Turbulence* (8), N6.
- KRAVCHENKO, A.G. & MOIN, P. 2000 Numerical studies of flow over a circular cylinder at $re_d = 3900$. *Physics of fluids* **12** (2), 403–417.
- LEE, J., CHOI, H. & PARK, N. 2010 Dynamic global model for large eddy simulation of transient flow. *Physics of Fluids* **22** (7), 075106.
- LEHMKUHL, O, RODRÍGUEZ, I, BORRELL, RICARD, CHIVA, J & OLIVA, A 2014 Unsteady forces on a circular cylinder at critical reynolds numbers. *Physics of Fluids* **26** (12), 125110.
- LOZANO-DURÁN, ADRIÁN & BAE, HYUNJI JANE 2019 Characteristic scales of townsend’s wall-attached eddies. *Journal of fluid mechanics* **868**, 698–725.
- MARIOTTI, A, BURESTI, G & SALVETTI, MV 2019 Separation delay through contoured transverse grooves on a 2d boat-tailed bluff body: Effects on drag reduction and wake flow features. *European Journal of Mechanics-B/Fluids* **74**, 351–362.
- MIHAILOVIC, J & CORKE, TC 1997 Three-dimensional instability of the shear layer over a circular cylinder. *Physics of Fluids* **9** (11), 3250–3257.
- MOHEBI, M., DU PLESSIX, P., MARTINUZZI, R.J. & WOOD, D.H. 2017 Effect of thickness-to-chord ratio on the wake of two-dimensional rectangular cylinders. *Physical Review Fluids* **2** (6), 064702.
- MOUSSAED, CARINE, SALVETTI, MARIA VITTORIA, WORNOM, STEPHEN, KOOBUS, BRUNO & DERVIEUX, ALAIN 2014 Simulation of the flow past a circular cylinder in the supercritical regime by blending rans and variational-multiscale les models. *Journal of Fluids and Structures* **47**, 114–123.
- NORBERG, CHRISTOFFER 1987 Effects of reynolds number and a low-intensity freestream turbulence on the flow around a circular cylinder. *Chalmers University, Goteborg, Sweden, Technological Publications* **87** (2), 1–55.
- NORBERG, CHRISTOFFER 2003 Fluctuating lift on a circular cylinder: review and new measurements. *Journal of Fluids and Structures* **17** (1), 57–96.

- OKAMOTO, SATORU, HIROSE, TATSUZO & ADACHI, TSUTOMU 1981 The effect of sound on the vortex-shedding from a circular cylinder: Acoustical vibrations directed along axis of cylinder. *Bulletin of JSME* **24** (187), 45–53.
- PARK, N., LEE, S., LEE, J. & CHOI, H. 2006 A dynamic subgrid-scale eddy viscosity model with a global model coefficient. *Physics of Fluids* **18** (12), 125109.
- PAULEY, LAURA L, MOIN, PARVIZ & REYNOLDS, WILLIAM C 1990 The structure of two-dimensional separation. *Journal of fluid Mechanics* **220**, 397–411.
- PFEIL, H & ORTH, U 1990 Boundary-layer transition on a cylinder with and without separation bubbles. *Experiments in fluids* **10** (1), 23–32.
- POPE, S.B. 2000 *Turbulent Flows*, pp. 147–148. Cambridge University Press.
- PORTELA, F ALVES, PAPADAKIS, G & VASSILICOS, JC 2018 Turbulence dissipation and the role of coherent structures in the near wake of a square prism. *Physical Review Fluids* **3** (12), 124609.
- PRASAD, ANIL & WILLIAMSON, CHARLES HK 1997 The instability of the shear layer separating from a bluff body. *Journal of fluid mechanics* **333**, 375–402.
- RODRÍGUEZ, I, LEHMKUHL, O, CHIVA, J, BORRELL, RICARD & OLIVA, A 2015 On the flow past a circular cylinder from critical to super-critical reynolds numbers: Wake topology and vortex shedding. *International Journal of Heat and Fluid Flow* **55**, 91–103.
- ROSHKO, A. 1954 On the drag and shedding frequency of two-dimensional bluff bodies. *Tech. Rep.* NACA-TN-3169. National advisory committee for aeronautics.
- SCHEWE, G. 1983 On the force fluctuations acting on a circular cylinder in crossflow from subcritical up to transcritical reynolds numbers. *Journal of fluid mechanics* **133**, 265–285.

- SHI, X.-D. & FENG, L.-H. 2015 Control of flow around a circular cylinder by bleed near the separation points. *Experiments in Fluids* **56** (12), 1–17.
- SIMMONS, JEL 1977 Similarities between two-dimensional and axisymmetric vortex wakes. *Aeronautical Quarterly* **28** (1), 15–20.
- SON, O. & CETINER, O. 2016 Drag prediction in the near wake of a circular cylinder based on dpiv data. *Journal of Applied Fluid Mechanics* **9** (4), 1963–1968.
- TENNEKES, H. & LUMLEY, J.L. 1972 *A First Course in Turbulence*, pp. 112–113. MIT Press.
- TOWNSEND, A.A. 1956 *The structure of turbulent shear flow*, chap. 7. Cambridge University Press.
- VAZ, GUILHERME, MABILAT, CHRISTOPHE, VAN DER WAL, REMMELT & GALLAGHER, PAUL 2007 Viscous flow computations on a smooth cylinders: a detailed numerical study with validation. In *International Conference on Offshore Mechanics and Arctic Engineering*, , vol. 4269, pp. 849–860.
- WEI, TAO & SMITH, CR 1986 Secondary vortices in the wake of circular cylinders. *Journal of Fluid Mechanics* **169**, 513–533.
- WEIDMAN, PATRICK D 1968 Wake transition and blockage effects on cylinder base pressures. PhD thesis, California Institute of Technology.
- WEN, C.-Y., YEH, C.-L., WANG, M.-J. & LIN, C.-Y. 2004 On the drag of two-dimensional flow about a circular cylinder. *Physics of Fluids* **16** (10), 3828–3831.
- WIESELSBERGER, C. 1922 Further information on the laws of fluid resistance. *Tech. Rep.* NACA-TN-121. National advisory committee for aeronautics.
- WILLIAMSON, C.H.K. 1992 The natural and forced formation of spot-like ‘vortex dislocations’ in the transition of a wake. *Journal of Fluid Mechanics* **243**, 393–441.
- WILLIAMSON, CHARLES HK 1996 Vortex dynamics in the cylinder wake. *Annual review of fluid mechanics* **28** (1), 477–539.
- XU, Y.-Z., FENG, L.-H. & WANG, J.-J. 2015 Experimental investigation on

- the flow over normal flat plates with various corner shapes. *Journal of Turbulence* **16** (7), 607–616.
- YEON, SEONG MO, YANG, JIANMING & STERN, FREDERICK 2016 Large-eddy simulation of the flow past a circular cylinder at sub-to super-critical reynolds numbers. *Applied Ocean Research* **59**, 663–675.
- ZAMAN, KBMQ & HUSSAIN, AKMF 1980 Vortex pairing in a circular jet under controlled excitation. part 1. general jet response. *Journal of fluid mechanics* **101** (3), 449–491.
- ZHOU, X., WANG, J.J. & HU, Y. 2019 Experimental investigation on the flow around a circular cylinder with upstream splitter plate. *Journal of Visualization* **22** (4), 683–695.
- ZHOU, Y., ALAM, M.M., YANG, H.X., GUO, H. & WOOD, D.H. 2011 Fluid forces on a very low reynolds number airfoil and their prediction. *International Journal of Heat and Fluid Flow* **32** (1), 329–339.

저임계, 임계, 초임계 영역에서의 원형 실린더 주위 유동: 비정상 유동 특성과 항력 모델링

서울대학교 대학원
기계항공공학부
진도현

요 약

본 연구에서는 원형 실린더 주위 유동에 대해 고정밀 수치해석을 수행하여 비정상 유동 특성을 분석하고 항력계수 예측 모델을 제안하였다.

제 1장에서는 가상 경계방법을 적용하여 저임계, 임계, 초임계 영역의 원형 실린더 유동에 대한 큰 에디 모사를 수행하였다. 해석에 사용한 레이놀즈 수는 저임계 영역에서는 60000, 임계 영역에서는 250000과 380000, 초임계 영역에서는 850000이다. 본 시뮬레이션의 결과로 얻은 항력계수와 스트로우할 수는 기존 연구와 잘 일치한다. 저임계 영역에서는 유동 박리점 이후에서 음의 기울기를 갖는 표면압력분포를 관찰하였다. 이 표면 부근에서 칼만 와류가 발달하는 것을 위상 평균된 유동장으로부터 확인하였고, 이때 칼만 와류의 중심에서 압력의 최소값을 관찰하였다. 반면 임계 및 초임계

영역에서는 유동 박리 후 비교적 넓은 영역에서 표면압력의 회복이 발생하였다. 이 영역들에서 칼만 와류 내 위상 평균된 압력은 저임계 영역에서의 압력보다 더 높았다. 박리점 직후에 발생하는 전단층 와류의 주파수는 레이놀즈 수가 증가함에 따라 증가하였고 박리점에서의 외부 방위각 속도 및 운동량 두께로 무차원화하면 레이놀즈 수에 관계없이 거의 일정하였다.

제 2장에서는 실린더의 항력계수에 대한 두 가지 예측 모델을 제안하였다. 첫 번째 모델은 주유동방향 측정 위치에서의 주유동방향 평균 속도와 레이놀즈 수직 응력 정보로부터 항력계수를 예측한다. 압력 분포의 영향을 모델링하기 위해 경계층 근사를 후류 영역에서 사용하고 베르누이 방정식을 비점성 영역에서 적용하였다. 3차원 비정상 시뮬레이션 결과로부터 얻은 유동장 정보에 본 모델을 적용해보니 시뮬레이션으로부터 얻은 항력 계수와 모델로 예측한 항력 계수가 잘 일치하였다. 또 다른 모델은 칼만 와류 형성에 대한 새로운 특성 스케일들을 정의하고 이를 기반으로 제안하였다. 속도, 전압력 그리고 길이에 대한 특성 스케일은 각각 중심선에서의 주유동방향 평균 속도 결손, 평균 전압 결손 그리고 후류 절반 너비이다. 이 스케일들로부터 항력 계수의 예측 모델을 추가적으로 제안하였을 뿐 아니라 보편 스트로우할 수 또한 제시하였다. 그리고 시뮬레이션 결과에 의해 검증된 추가 가정으로 항력 계수, 스트로우할 수 및 기저 압력 계수 간의 관계를 설명하는 스케일링 법칙을 유도하였다. 원형 실린더 이외의 다른 2차원 형상의 데이터를 본 스케일링 법칙에 적용하였으며, 데이터들이 본 스케일링 법칙에 잘 부합하는 것을 확인하였다.

주요어: 원형 실린더, 후류, 칼만 와류, 스케일링법칙, 항력 모델

학 번: 2013-22501